

# Keck telescope constraint on cosmological variation of the proton-to-electron mass ratio

A. L. Malec,<sup>1\*</sup> R. Buning,<sup>2</sup> M. T. Murphy,<sup>1</sup> N. Milutinovic,<sup>3</sup> S. L. Ellison,<sup>3</sup>  
J. X. Prochaska,<sup>4</sup> L. Kaper,<sup>2,5</sup> J. Tumlinson,<sup>6</sup> R. F. Carswell,<sup>7</sup> W. Ubachs<sup>2</sup>

<sup>1</sup>Centre for Astrophysics and Supercomputing, Swinburne University of Technology, Melbourne, Victoria 3122, Australia

<sup>2</sup>Laser Centre, VU University, De Boelelaan 1081, 1081 HV Amsterdam, The Netherlands

<sup>3</sup>Department of Physics and Astronomy, University of Victoria, Victoria, BC, V8P 1A1, Canada

<sup>4</sup>University of California Observatories – Lick Observatory, University of California, Santa Cruz, CA 95064

<sup>5</sup>Astronomical Institute Anton Pannekoek, Universiteit van Amsterdam, 1098 SJ Amsterdam, The Netherlands

<sup>6</sup>Yale Center for Astronomy and Astrophysics, Department of Physics, New Haven, CT 06520, USA

<sup>7</sup>Institute of Astronomy, University of Cambridge, Madingley Road, Cambridge, CB3 0HA, UK

Accepted 2009 December 14. Received 2009 November 18; in original form 2009 June 9

## ABSTRACT

Molecular transitions recently discovered at redshift  $z_{\text{abs}} = 2.059$  toward the bright background quasar J2123–0050 are analysed to limit cosmological variation in the proton-to-electron mass ratio,  $\mu \equiv m_p/m_e$ . Observed with the Keck telescope, the optical echelle spectrum has the highest resolving power and largest number (86) of  $\text{H}_2$  transitions in such analyses so far. Also, (seven) HD transitions are used for the first time to constrain  $\mu$ -variation. These factors, and an analysis employing the fewest possible free parameters, strongly constrain  $\mu$ 's relative deviation from the current laboratory value:  $\Delta\mu/\mu = (+5.6 \pm 5.5_{\text{stat}} \pm 2.9_{\text{sys}}) \times 10^{-6}$ , indicating an insignificantly larger  $\mu$  in the absorber. This is the first Keck result to complement recent null constraints from three systems at  $z_{\text{abs}} > 2.5$  observed with the Very Large Telescope. The main possible systematic errors stem from wavelength calibration uncertainties. In particular, distortions in the wavelength solution on echelle order scales are estimated to contribute approximately half the total systematic error component, but our estimate is model dependent and may therefore under or overestimate the real effect, if present.

To assist future  $\mu$ -variation analyses of this kind, and other astrophysical studies of  $\text{H}_2$  in general, we provide a compilation of the most precise laboratory wavelengths and calculated parameters important for absorption-line work with  $\text{H}_2$  transitions redwards of the hydrogen Lyman limit.

**Key words:** atomic data – line: profiles – techniques: spectroscopic – methods: data analysis – quasars: absorption lines

## 1 INTRODUCTION

The Standard Model of particle physics is parametrized by several dimensionless ‘fundamental constants’, such as coupling constants and mass ratios, whose values are not predicted by the Model itself. Instead their values and, indeed, their constancy must be established experimentally. If found to vary in time or space, understanding their dynamics may require a more fundamental theory, perhaps one unifying the four known physical interactions. Two such parameters whose constancy can be tested to high precision are the fine-structure constant,  $\alpha \equiv e^2/4\pi\epsilon_0\hbar c$ , characterising electromagnetism's strength, and the proton-to-electron mass ratio,  $\mu \equiv m_p/m_e$  – effectively the ratio of the strong and electro-weak scales. Grand Unified Theories can predict relationships between variations in  $\mu$

and  $\alpha$  (e.g. Calmet & Fritzsche 2002), but which parameter varies the most and whether in the same or opposite sense to the other is model-dependent (Dent et al. 2008).

Earth-bound laboratory experiments, conducted over several-year time-scales, which use ultra-stable lasers to compare different atomic clocks based on different atoms/ions (e.g. Cs,  $\text{Hg}^+$ ,  $\text{Al}^+$ ,  $\text{Yb}^+$ , Sr, Dy; e.g. Prestage et al. 1995; Marion et al. 2003; Peik et al. 2004; Cingöz et al. 2007), have limited  $\alpha$ 's time-derivative to  $\dot{\alpha}/\alpha = (-1.6 \pm 2.3) \times 10^{-17} \text{ yr}^{-1}$  (Rosenband et al. 2008). Combining results from similar experiments limits  $\mu$ 's time-derivative to  $\dot{\mu}/\mu = (-1.6 \pm 1.7) \times 10^{-15} \text{ yr}^{-1}$  (Blatt et al. 2008). A direct constraint was also recently obtained from a ro-vibrational transition in the  $\text{SF}_6$  molecule,  $\dot{\mu}/\mu = (-3.8 \pm 5.6) \times 10^{-14} \text{ yr}^{-1}$  (Shelkovnikov et al. 2008).

Important probes of variations over much larger space- and time-scales – up to  $\sim 90\%$  of the age of the Universe – are nar-

\* E-mail: amalec@swin.edu.au (ALM)

row absorption lines imprinted on the spectra of distant, background quasars by gas clouds associated with foreground galaxies (Bahcall et al. 1967). In particular, the Lyman and Werner transitions of molecular hydrogen (laboratory wavelengths  $\lambda_{\text{lab}} \lesssim 1150 \text{ \AA}$ ), by far the most abundant molecule in the Universe, are useful  $\mu$ -variation indicators at cosmological redshifts  $z > 2$  where they are detectable with ground-based telescopes (Thompson 1975; Varshalovich & Levshakov 1993).

Variations in  $\mu$  should shift the ro-vibronic transition frequencies in molecular spectra. This mass-dependent shift is quantified by a sensitivity coefficient,  $K_i$ , for each transition  $i$ . Consider a single transition arising in an absorption cloud whose redshift is established to be  $z_{\text{abs}}$  from other transitions which are insensitive to variations in  $\mu$ . If  $\mu$  was the same in the absorption cloud as in the laboratory, we would expect to find transition  $i$  at wavelength  $\lambda_{\text{lab}}^i(1 + z_{\text{abs}})$ . If instead we measure it to be at wavelength  $\lambda_i = \lambda_{\text{lab}}^i(1 + z_i)$  (i.e. at redshift  $z_i \neq z_{\text{abs}}$ ), then the shift in redshift,  $\Delta z_i \equiv z_i - z_{\text{abs}}$ , or velocity,  $\Delta v_i$ , can be ascribed to a variation in  $\mu$ ,

$$\frac{\Delta v_i}{c} \approx \frac{\Delta z_i}{1 + z_{\text{abs}}} = K_i \frac{\Delta \mu}{\mu}, \quad (1)$$

where  $\Delta \mu / \mu \equiv (\mu_z - \mu_{\text{lab}}) / \mu_{\text{lab}}$  for  $\mu_{\text{lab}}$  and  $\mu_z$  the current laboratory value of  $\mu$  and its value in the absorption cloud at redshift  $z$ , respectively. That different transitions have different  $K$  values enables a differential measurement of  $\Delta \mu / \mu$  from two or more transitions. That is, it allows the redshift  $z_{\text{abs}}$  to be determined simultaneously with  $\Delta \mu / \mu$ .

Indications for a significantly positive  $\Delta \mu / \mu$  have been derived from two  $\text{H}_2$ -bearing quasar absorbers observed with the Ultraviolet and Visual Echelle Spectrograph (UVES) on the ESO Kueyen Very Large Telescope (VLT) in Chile. Ivanchik et al. (2005) studied high resolving power ( $R \approx 53000$ ), high signal-to-noise ratio ( $\text{SNR} \approx 30\text{--}70$ ) UVES spectra of the  $z_{\text{abs}} = 2.595$  and  $3.025$  absorbers towards the quasars Q0405–443 and Q0347–383, respectively. They used a total of 76  $\text{H}_2$  lines in the two spectra, fitting them ‘line-by-line’ – i.e. independently of each other – to derive values for  $\lambda_i$ . In this analysis the  $\text{H}_2$  absorption profiles in Q0347–383 were treated as comprising a single cloud. Of the two resolved  $\text{H}_2$  features observed in Q0405–443, only the strongest was fitted. Using two different sets of  $\text{H}_2$  laboratory wavelengths (Abgrall et al. 1993 and Philip et al. 2004) Ivanchik et al. derived two sets of  $z_i$  values which yielded two  $\Delta \mu / \mu$  values,  $(+30.5 \pm 7.5) \times 10^{-6}$  and  $(+16.5 \pm 7.4) \times 10^{-6}$  respectively.

Reinhold et al. (2006) subsequently improved the laboratory wavelengths and the calculation of the  $K$  sensitivity coefficients (see Sections 2.2 and 2.3). Using the same values of  $\lambda_i$  and their uncertainties derived by Ivanchik et al. (2005), Reinhold et al. performed a ‘line-by-line’ analysis to refine the values of  $\Delta \mu / \mu$  for each absorber:  $(+20.6 \pm 7.9) \times 10^{-6}$  for Q0347–383 and  $(+27.8 \pm 8.8) \times 10^{-6}$  for Q0405–443. The combined value of  $(+24.5 \pm 5.9) \times 10^{-6}$  was presented as an *indication* for cosmological variation in  $\mu$ .

King et al. (2008) reanalysed the same raw UVES quasar spectra with improved flux extraction and, more importantly, using the improved wavelength calibration procedures detailed in Murphy et al. (2007). King et al. used slightly more  $\text{H}_2$  transitions and a ‘simultaneous fitting’ technique with explicit treatment of Lyman- $\alpha$  forest lines (see Section 3.1) to constrain the values of  $\Delta \mu / \mu$  in the newly reduced and calibrated spectra. They found decreased values in both absorbers compared to previous works:  $\Delta \mu / \mu = (+8.2 \pm 7.4) \times 10^{-6}$  and  $(+10.1 \pm 6.2) \times 10^{-6}$  for Q0347–383 and Q0405–443 respectively. King et al. also anal-

ysed 64  $\text{H}_2$  lines of a third absorption system, that at  $z_{\text{abs}} = 2.811$  towards Q0528–250, using UVES spectra with  $R \approx 45000$  and  $\text{SNR} \approx 25\text{--}45$ . This provided the tightest constraint of all three absorbers:  $\Delta \mu / \mu = (-1.4 \pm 3.9) \times 10^{-6}$ . Thus, the combined result, where the slightly positive values for Q0347–383 and Q0405–443 are somewhat cancelled by the slightly negative but more precise value for Q0528–250, was a null constraint of  $\Delta \mu / \mu = (+2.6 \pm 3.0) \times 10^{-6}$ . The same UVES spectra were also recently studied by Wendt & Reimers (2008) and Thompson et al. (2009) using different data reduction and analysis techniques, generally aimed at avoiding and/or understanding potential systematic errors and biases in  $\Delta \mu / \mu$ . They also find null constraints, albeit with somewhat larger statistical errors than King et al. due to their more conservative approaches.

So, while some analyses indicate a varying  $\mu$  (e.g. Reinhold et al. 2006), recent reanalyses of the three well-documented and high-quality  $\text{H}_2$  absorption spectra at  $z > 2$  do not provide evidence for cosmological variation in  $\mu$ . A much larger statistical sample is desirable, deriving from several telescopes and spectrographs, for definitive results and to provide measurements over a larger redshift range. However, the scarcity of known  $\text{H}_2$  absorbers hampers such progress:  $>1000$  absorption systems rich in neutral hydrogen – i.e. damped Lyman- $\alpha$  systems, with  $\text{H I}$  column densities  $N(\text{H I}) \geq 2 \times 10^{20} \text{ cm}^{-2}$  – are known (e.g. Prochaska & Wolfe 2009) but systematic searches for  $\text{H}_2$  have been conducted in  $<100$  systems (e.g. Ledoux et al. 2003) and only  $\sim 15$  are known to harbour detectable column densities of  $\text{H}_2$  (Noterdaeme et al. 2008). Furthermore, for varying- $\mu$  analyses,  $\text{H}_2$  absorbers must be (i) at  $z > 2$  to shift enough Lyman and Werner transitions above the atmospheric cutoff ( $\sim 3000 \text{ \AA}$ ), (ii) have bright background quasars to enable high-SNR, high resolution spectroscopy and, (iii) have high enough  $\text{H}_2$  column densities so that individual transitions absorb significant fractions of the quasar continuum.

In these respects, and others, the newly discovered absorber studied here – at  $z_{\text{abs}} = 2.059$  towards the  $z_{\text{em}} = 2.261$  quasar SDSS J212329.46–005052.9 (hereafter J2123–0050; Milutinovic et al., in preparation) – is exceptional. It is the first studied with the High Resolution Echelle Spectrometer (HIRES; Vogt et al. 1994) on the Keck telescope in Hawaii to provide constraints of similar precision to the three VLT ones<sup>1</sup>. J2123–0050 is unusually bright ( $r$ -band magnitude  $\approx 16.5$  mag), providing a high SNR spectrum in just 6 hours observation with, importantly, the highest spectral resolution for an  $\text{H}_2$  absorber to date:  $R \approx 110000$  or full-width-at-half-maximum FWHM  $\approx 2.7 \text{ km s}^{-1}$ . HIRES’s high ultraviolet (UV) throughput provides 86  $\text{H}_2$  transitions for constraining  $\mu$ -variation, the largest number in an individual absorber so far. Also, for the first time, (7) HD transitions are used to constrain  $\mu$ -variation; HD has been observed in just two other high-redshift absorbers (Varshalovich et al. 2001; Noterdaeme et al. 2008).

This paper is organised as follows. The data required for our analysis – the Keck spectrum of J2123–0050, laboratory  $\text{H}_2$ /HD transition wavelengths and the sensitivity coefficients – are described in Section 2. Section 3 presents our analysis technique and main result while in Section 4 we conduct a variety of internal consistency checks and consider the most important systematic errors.

<sup>1</sup> Cowie & Songaila (1995) previously analysed Keck/HIRES spectra of Q0528–250 to derive a comparatively weak constraint of  $\Delta \mu / \mu = (-80 \pm 313) \times 10^{-6}$ .

We conclude with a comparison of our results with others in the literature in Section 5.

## 2 DATA

### 2.1 Keck spectrum of J2123–0050

Full details of the Keck/HIRES observations of J2123–0050 are provided in Milutinovic et al. (in preparation) who study the physical conditions and elemental abundances in the  $z_{\text{abs}} = 2.059$  absorber. Here we present only the features of the spectral data reduction and the final spectrum which are important for the varying- $\mu$  analysis.

The HIRES observations comprised 2 sets of 3×1-hr exposures of J2123–0050 taken on consecutive nights (2007 August 19 & 20). The seeing was very good, just 0".3–0".5 at  $\sim 6000$  Å (where the guide camera is sensitive), and so a 0".4-wide slit was used. A single thorium–argon (ThAr) lamp exposure calibrated each set of three quasar exposures; the ThAr exposure was taken immediately before or after each quasar set. Spectrograph temperature and atmospheric pressure shifts between the quasar and ThAr exposures were  $< 1$  K and  $< 1$  mbar respectively.

The raw spectra were reduced using the `HIREDUX` software<sup>2</sup> written and maintained by one of us (JXP). The flux extraction procedure also calculates the formal statistical flux error spectrum for each echelle order. Particular attention was paid to accurate wavelength calibration. ThAr lines were pre-selected with the procedures described in Murphy et al. (2007) and improvements were made to the ThAr line fitting in `HIREDUX` to ensure that reliable centroids for the ThAr lines were determined. The ThAr flux was extracted using the same spatial profile weights as the corresponding quasar extraction. The root-mean-square (RMS) of the wavelength calibration residuals was  $\sim 80$  m s<sup>−1</sup>; that is, the calibration at any given wavelength has RMS error  $\sim 80$  m s<sup>−1</sup>. The resolving power was measured from the extracted ThAr spectra to be  $R \approx 110000$ . During extraction, the spectra were re-binned to a common vacuum-heliocentric wavelength scale with a dispersion of  $1.3$  km s<sup>−1</sup> pixel<sup>−1</sup>. They were combined to form a final spectrum for subsequent analysis using the `UVES_POPLER` software<sup>3</sup> written and maintained by one of us (MTM).

The final spectrum of J2123–0050 covers (vacuum-heliocentric) wavelengths 3071–5896 Å. An initial global quasar continuum was constructed using simple polynomial fits. The details of this process are unimportant because the local continuum was modelled and fitted simultaneously with most H<sub>2</sub>/HD and Lyman- $\alpha$  forest absorption lines. That is, the initial global continuum is just a nominal, fixed starting guess for most molecular transitions. All the H<sub>2</sub>/HD transitions fall bluewards of 3421 Å where the SNR in the nominal continuum ranged from 7 per  $1.3$  km s<sup>−1</sup> pixel at  $\sim 3075$  Å to 25 at  $\sim 3420$  Å. We made a final, manual check on the data quality in the spectral region around each H<sub>2</sub>/HD transition. In particular, we ensured that the data contributed by the different exposures agreed to within the uncertainty expected from the individual flux error arrays derived during the extraction procedure. This is also a check that the statistical uncertainties fairly estimate the RMS flux variations in the final spectrum. Also, no significant wavelength or velocity shifts between the individual spectra were apparent.

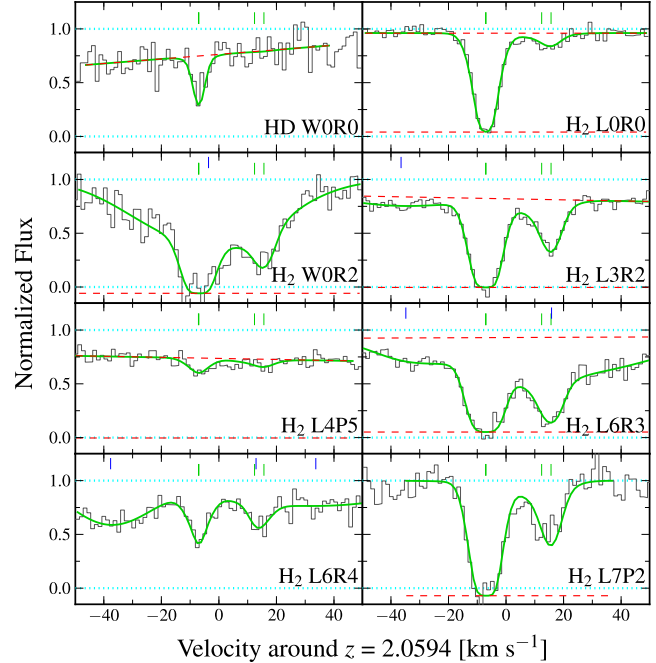


**Figure 2.** Some of the 86 H<sub>2</sub> and 7 HD lines from the J2123–0050 Keck spectrum on a velocity scale centred at  $z_{\text{abs}} = 2.0594$ . The spectrum (black histogram) is normalized by a nominal continuum (upper dotted line). Local linear continua (upper dashed lines) and zero levels (lower dashed lines) are fitted simultaneously with the molecular and broader Lyman- $\alpha$  lines, the positions of which are indicated with, respectively, lighter and darker tick marks (offset vertically from each other) above the spectrum. The 4-component fiducial fit is the solid curve. Note that the two left-most components are nearly coincident in velocity.

Figure 1 shows the region of the final spectrum containing H<sub>2</sub>/HD lines (3071–3421 Å) and a region redwards of the Lyman- $\alpha$  emission line (4905–4926 Å) containing metal lines which are required in our fit described in Section 3.1.

Figure 2 highlights some of the H<sub>2</sub> and HD transitions covering the observed range of overall line-strengths, SNRs and ground-state rotational levels, characterised by the quantum number  $J$  (‘ $J$ -levels’). H<sub>2</sub> lines are observed in the  $B^1\Sigma_u^+ - X^1\Sigma_g^+$  Lyman and  $C^1\Pi_u - X^1\Sigma_g^+$  Werner bands, for  $J \in [0, 5]$ . HD is observed in six R0 Lyman lines and one R0 Werner line. The molecular absorption shows two distinct spectral features (SFs), separated by  $\approx 20$  km s<sup>−1</sup>. Figure 1 shows that the strong left-hand SF appears saturated for most low- $J$  transitions, while the weaker right-hand SF appears unsaturated in almost all transitions. Only the left-hand SF is detected in the HD transitions. Clearly, accurately recovering  $\Delta\mu/\mu$  with the maximum precision available from the spectrum must take into account this non-trivial absorption profile, the strength of which varies from transition to transition, while also allowing the varying SNRs, degrees of Lyman- $\alpha$  blending, and possible continuum-placement errors to contribute to the final uncertainty on  $\Delta\mu/\mu$ . We achieve this with a simple  $\chi^2$  fitting technique combined with a detailed model of the absorption profile in Section 3.1.

### 2.2 Laboratory wavelengths for H<sub>2</sub> and HD transitions

Equation (1) states that velocity shifts between different H<sub>2</sub>/HD transitions can be related to a varying  $\mu$ . But it assumes that the current laboratory wavelengths of those transitions are known to

<sup>2</sup> <http://www.ucoick.org/~xavier/HIREDUX>

<sup>3</sup> [http://astronomy.swin.edu.au/~mmurphy/UVES\\_popler.html](http://astronomy.swin.edu.au/~mmurphy/UVES_popler.html)

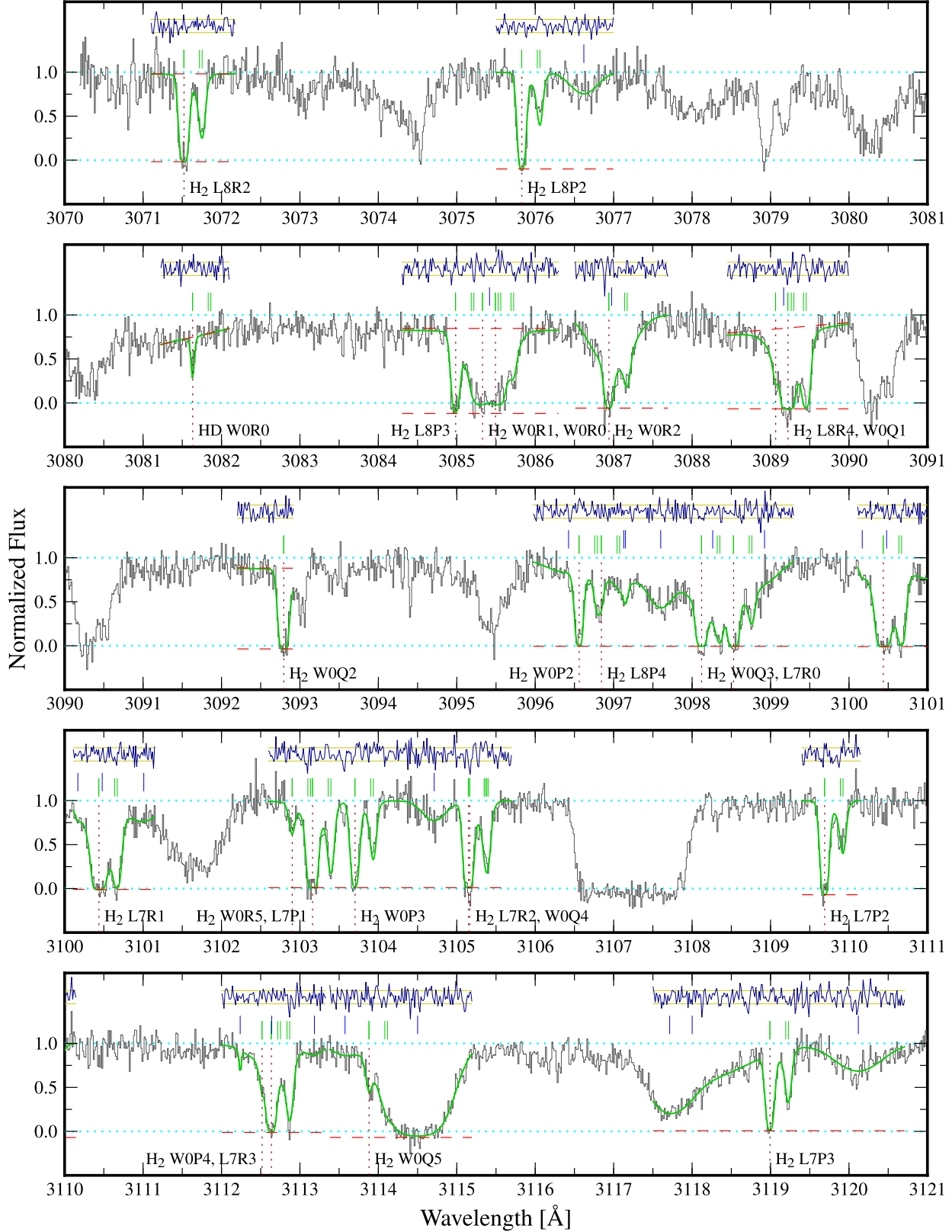


**Figure 1.** All regions of the J2123–0050 Keck spectrum fitted simultaneously in our analysis. Here we show only 5 of the 37 panels comprising the full figure; the other panels are available in the electronic version of this paper. The spectrum (black histogram) is normalized by a nominal continuum (upper dotted line) fitted over large spectral scales. Local linear continua (upper dashed lines) and zero levels (lower dashed lines) are fitted simultaneously with the H<sub>2</sub>/HD and broader Lyman- $\alpha$  lines. The fits are shown with solid grey/green lines. H<sub>2</sub>/HD transitions are labelled and their constituent velocity components are indicated by grey/green tick-marks immediately above the spectrum. Higher above the spectrum are tick-marks indicating the positions of Lyman- $\alpha$  lines (dark-grey/blue) and Fe II lines (lighter grey/red). Note that the metal-line velocity structure is constrained with the Fe II  $\lambda 1608$  Å transition shown in the final panel of the figure (i.e. in the electronic version). The residual spectrum (i.e. [data] – [fit]), normalized to the 1- $\sigma$  errors (faint, horizontal solid lines), is shown above the tick-marks.



high enough precision to be considered exact compared to the precision available from the astronomical spectra. And with wavelengths  $\lambda_{\text{lab}} \lesssim 1150 \text{ \AA}$ , laboratory measurements of these transitions are challenging. Nevertheless, the laboratory measurements have improved over the years and now provide accurate and precise laboratory wavelengths for all the  $\text{H}_2/\text{HD}$  transitions detected in our spectrum of J2123–0050 and, more generally, for those relevant in  $\mu$ -variation studies.

While the classical data of the Meudon group reached fractional wavelength accuracies of  $\delta\lambda/\lambda \sim 10^{-6}$  (Abgrall et al. 1993), the first laser calibration study using a pulsed dye laser system (Hinnen et al. 1994) reached similar or somewhat improved accuracies of  $6 \times 10^{-7}$ . The implementation of Fourier transform-limited laser pulses in the harmonic conversion processes (Ubachs et al. 1997) allowed an order of magnitude improvement. Using this technique, several subsequent studies provided a data set of Lyman and Werner transition wavelengths with fractional accuracies of  $5 \times 10^{-8}$  (Philip et al. 2004; Ubachs & Reinhold 2004). Recently, even more accurate values – fractional accuracies of  $5 \times 10^{-9}$  for most Lyman transitions and  $1\text{--}2 \times 10^{-8}$  for Werner transitions – were obtained from combining two-photon excitation results with Fourier-transform studies of emission lines between  $\text{H}_2$  excited states (Salumbides et al. 2008).

In our analysis we use the most accurate wavelength from these studies for each  $\text{H}_2$  transition detected in our spectrum of J2123–0050. Table 1 compiles the most precise laboratory data into a complete, up-to-date catalogue for all allowed Lyman and Werner  $\text{H}_2$  transitions between the lowest 8 rotational levels in the ground and excited states with wavelengths generally above the hydrogen Lyman limit (more specifically, to the first 20 and 6 excited vibrational levels for Lyman and Werner transitions, respectively). Most important to  $\mu$ -variation studies like ours are the wavelengths and sensitivity coefficients (see below), but we have also included the other laboratory data required for fitting the  $\text{H}_2$  absorption lines seen in astronomical spectra, such as oscillator strengths. And while we detect only a small subset of these  $\text{H}_2$  transitions in our spectrum of J2123–0050, we include a complete list in Table 1 as a useful reference catalogue for other astronomical studies.

The HD transitions were recently measured via direct extreme UV laser excitation to a relative accuracy of  $\approx 5 \times 10^{-8}$  by Hollenstein et al. (2006) and Ivanov et al. (2008) and we use those values here. Table 2 provides the laboratory data for the 10 HD transitions falling in our spectrum, 7 of which we use in our analysis.

### 2.3 Sensitivity coefficients, $K$

The  $K$  coefficients used here were calculated via a semi-empirical analysis (Ubachs et al. 2007). In this approach a Dunham representation of the ground and excited state level structure is derived from fits to the accurately determined transition frequencies. In the first instance, the levels most heavily perturbed by rotational-electronic interactions are excluded. Known mass-scaling laws for the Dunham coefficients then yield the  $K$  coefficients. The non-adiabatically perturbed levels were treated in the second instance, taking into account wave function mixing of levels in the  $\text{B}^1\Sigma_u^+$  and  $\text{C}^1\Pi_u$  systems. Small adiabatic corrections (at the 1 per cent level) were included as well. We note here that the values reported in Ubachs et al. (2007) include additional mass-dependent effects on the non-adiabatic interaction matrix elements that were not included in the initial study of Reinhold et al. (2006); differences be-

**Table 1.** Catalogue of the most accurate and precise laboratory parameters for fitting  $\text{H}_2$  absorptions lines. Represented are all allowed Lyman and Werner  $\text{H}_2$  transitions between the lowest 8 rotational levels in the ground and excited states with excited state vibrational quantum numbers up to 20 and 6 for Lyman and Werner transitions, respectively. The first column provides a short-hand notation for the transition: letters denote a Lyman (L) or Werner (W) line and the branch, where P, Q and R represent  $J' - J = -1$ , 0 and 1, respectively, for  $J$  and  $J'$  the ground state and excited state  $J$ -levels, respectively; the first integer is the excited state vibrational quantum number and the second is  $J$ . The second column gives the most precise reported laboratory wavelength and its  $1\text{-}\sigma$  uncertainty and the third column provides the reference: 1 = Bailly et al. (2009), 2 = Ubachs et al. (2007) (a suffix “a” refers to directly measured wavelengths while “b” refers to wavelengths calculated from directly measured lines via combination differences) and 3 = Abgrall et al. (1993) for the excited state energy levels with ground states derived directly from Jennings et al. (1984). Note that wavelengths with reference 3 are much less precise than those from references 1 and 2. The fourth column gives the oscillator strengths which were calculated from the Einstein  $A$  coefficients given by Abgrall et al. (1994). The fifth column gives the (natural) damping coefficients which were calculated from the total transition probabilities ( $A_{\text{t}}$ ) in Abgrall et al. (2000). The final column gives the sensitivity coefficients calculated in Ubachs et al. (2007) which have estimated uncertainties of typically  $< 5 \times 10^{-4}$  (see text). Only a small excerpt from the full table is presented here; the full table is available in the electronic version of this paper.

Trans- ition	$\lambda_{\text{lab}}$ [Å]	Ref.	$f$ [ $10^{-2}$ ]	$\Gamma$ [ $10^9 \text{ s}^{-1}$ ]	$K$
L0P1	1110.062558(3)	1	0.05739	1.87	−0.0097
L0P2	1112.495989(3)	1	0.06915	1.86	−0.0119
L0P3	1115.895530(3)	1	0.07381	1.86	−0.0149
L0P4	1120.248839(3)	1	0.07560	1.85	−0.0187
L0P5	1125.540690(5)	1	0.07577	1.84	−0.0233
L0P6	1131.753504(6)	1	0.07481	1.83	−0.0286
L0P7	1151.6384(14)	3	0.07299	1.82	−0.0345

**Table 2.** Laboratory data for  $J = 0$  HD transitions falling in (but not necessarily detected or fitted in) our spectrum of J2123–0050. The columns have the same descriptions as in Table 1 except for the following. The laboratory wavelength references are 4 = Hollenstein et al. (2006) and 5 = Ivanov et al. (2008). The oscillator strengths ( $f$ ) and damping coefficients ( $\Gamma$ ) were calculated from the Einstein  $A$  coefficients and total transition probabilities ( $A_{\text{t}}$ ), respectively, given by Abgrall & Roueff (2006). The sensitivity coefficients ( $K$ ) were calculated by Ivanov et al. (2008) and have estimated uncertainties of typically  $< 1.5 \times 10^{-4}$ .

Trans- ition	$\lambda_{\text{lab}}$ [Å]	Ref.	$f$ [ $10^{-2}$ ]	$\Gamma$ [ $10^9 \text{ s}^{-1}$ ]	$K$
L0R0	1105.840555(57)	4	0.07436	1.87	−0.0065
L1R0	1092.001264(58)	4	0.29669	1.76	−0.0004
L2R0	1078.831044(61)	4	0.67473	1.67	0.0053
L3R0	1066.27568(6)	5	1.14500	1.58	0.0106
L4R0	1054.29354(6)	5	1.63570	1.50	0.0156
L5R0	1042.85005(6)	5	2.05477	1.43	0.0201
L6R0	1031.91493(6)	5	2.35911	1.36	0.0244
L7R0	1021.46045(6)	5	2.53491	1.30	0.0283
L8R0	1011.46180(6)	5	2.61849	1.25	0.0319
L9R0	1001.89413(6)	5	2.47212	1.19	0.0353
W0R0	1007.29020(6)	5	3.25368	1.18	−0.0039

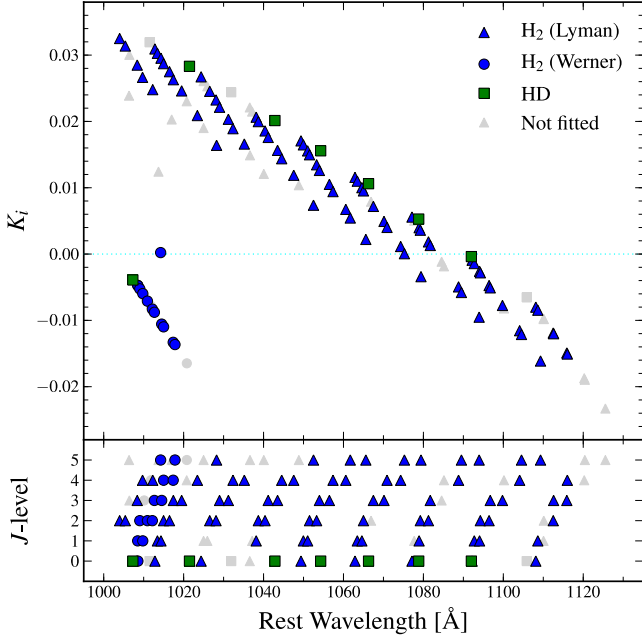


**Figure 3.** *Upper panel:* The sensitivity coefficients,  $K_i$ , for the  $J=0-5$  HD and H<sub>2</sub> Lyman and Werner transitions,  $i$ , used in our analysis (dark/coloured points) and those not detected or fitted (light grey points). The legend explains the symbols used in both panels. *Lower panel:* The distribution of transitions with wavelength according to their  $J$ -levels.

tween the two are nevertheless marginal. We also note that these  $K$  coefficients are in very good agreement with the independent *ab initio* calculations by Meshkov et al. (2006); the agreement within 1 per cent is reassuring for both methods, since it corresponds to the estimated uncertainties in both. The  $K$  coefficients for the H<sub>2</sub> transitions are included in Table 1. The  $K$  coefficients for HD were derived in *ab initio* calculations by Ivanov et al. (2008) and are given in Table 2.

Figure 3 (upper panel) shows the  $K$  values, which occupy the range  $-0.02 < K < +0.03$ , for all detected molecular transitions. Note the general increase in  $K$  for bluer Lyman transitions. Adding the Werner transitions below  $\lambda_{\text{lab}} = 1020$  Å provides a more complicated signature of a varying  $\mu$  because they shift in the opposite direction to the Lyman transitions at similar wavelengths. These aspects of Fig. 3 are particularly important when considering possible systematic effects in Section 4.2.

### 3 ANALYSIS AND RESULTS

#### 3.1 $\chi^2$ minimization analysis

If we knew *a priori* that molecular absorption occurred at a single redshift in a single cloud and no other absorption lines were present, measuring  $\Delta\mu/\mu$  would be straightforward: each molecular line's redshift could be determined from a fit against a well-defined background continuum and its relative deviation from some arbitrary redshift could be plotted against its  $K$  coefficient. Equation (1) implies that  $\Delta\mu/\mu$  would simply be the slope of such a plot. The offset would be degenerate with the arbitrary redshift itself (though it clearly should be fitted as a free parameter).

In reality, two main complicating factors are important. Firstly, all molecular lines fall in the Lyman- $\alpha$  forest, the series of

comparatively broad H I Lyman- $\alpha$  absorption lines randomly distributed in optical depth and redshift bluewards of the quasar's Lyman- $\alpha$  emission line. As Figs. 1 and 2 show, many molecular lines fall within the absorption profile of one or more forest lines, so the latter must also be fitted to provide an effective background. Secondly, the molecular lines show 'velocity structure' – several absorbing clouds with similar redshifts and different optical depths and Doppler widths. The two main spectral features (SFs) highlighted in Fig. 2 are obvious examples, but we demonstrate below that each SF comprises more than one absorbing 'velocity component' (VC).

The 'simultaneous fitting' technique we employ here optimally and robustly addresses these complications by fitting all detected H<sub>2</sub> and HD absorption profiles, together with the broader Lyman- $\alpha$  profiles, simultaneously in a single, comprehensive fit. Minimizing  $\chi^2$  allows uncertainties in the forest parameters – the effective continuum – to contribute naturally to uncertainties in  $\Delta\mu/\mu$ . Other advantages this technique brings over the earlier 'line-by-line' fitting approach are outlined by King et al. (2008).

#### 3.1.1 Free parameters and physical assumptions

Each absorption line is modelled as a Voigt profile – the convolution of Gaussian Doppler broadening and the transition's natural line-shape. The oscillator strength and natural line-width determine the latter; their values are provided in Tables 1 and 2. Three parameters describe each absorption cloud's properties: Doppler width,  $b$ , column density,  $N$ , and redshift,  $z_{\text{abs}}$ . This is the only consideration for the Lyman- $\alpha$  lines but different molecular transitions share these parameters in physically important ways.

For H<sub>2</sub> and HD, each  $J$ -level has a different ground state population, so all transitions from the same  $J$ -level have the same, single value of  $N$  in each VC. This is clearly also true for the  $b$  and  $z_{\text{abs}}$  values. However, we make the further assumption that the velocity structure is the same in all  $J$ -levels, i.e. that a given VC has the same  $z_{\text{abs}}$  value in all  $J$ -levels. We test the importance of this assumption in Section 4.2 and find that it has little impact on our results. We also assume that a given VC is characterised by the same, single value of  $b$  in all  $J$ -levels; we test the importance of this assumption in Section 4.1. In relating the absorption cloud parameters of different transitions in these physically meaningful ways, the number of free parameters is minimized. This is similar to the analysis in King et al. (2008), though they fitted the molecular oscillator strengths as free parameters as well. Finally, because the HD transitions are few and relatively weak – recall that only the left-hand spectral feature is detected – we further assume that the ratio of an HD VC's column density to that of the corresponding VC in the H<sub>2</sub>  $J=0$  transitions is the same for all VCs. As can be seen from Fig. 1, there is no strong evidence against this assumption, a conclusion corroborated by removing the HD transitions from the analysis altogether in Section 4.1.

There are several Fe II transitions with  $\lambda_{\text{lab}} < 1150$  Å near some H<sub>2</sub> transitions which, in the  $z_{\text{abs}} = 2.059$  absorber, appear quite weak but with velocity structure extending over  $\sim 400$  km s<sup>-1</sup>. The velocity components in these Fe II transitions are marked in Fig. 1. This velocity structure was strongly constrained by using the Fe II  $\lambda 1608$  Å transition, which falls redwards of the Lyman- $\alpha$  forest and so has a well-defined continuum. This transition was blended with weak, broad C IV  $\lambda 1550$  absorption associated with the quasar itself (Hamann et al., in preparation). The C IV  $\lambda 1550$  absorption was constrained by fitting the corresponding C IV  $\lambda 1548$  absorption. Thus, it was necessary to model both metal line species,

as shown in Fig. 1, to obtain a reliable model of the Fe II transitions appearing near our H<sub>2</sub> transitions of interest. The H<sub>2</sub> fits are insensitive to those of the metal lines.

As noted in Section 2.1, a nominal continuum was initially fitted to the Lyman- $\alpha$  forest region before establishing a detailed fit to the absorption lines. Simple, low-order polynomial fits connecting seemingly unabsorbed regions of the spectrum, typically spaced apart by  $\gtrsim 5000 \text{ km s}^{-1}$ , provided a qualitatively realistic continuum. However, *quantitatively* different continua were determined by different authors of this paper; the differences were large enough to slightly affect fits to individual absorption lines. And because our line fitting approach explicitly connects the properties of molecular lines to each other, it is important to recognise that this nominal, *fixed* quasar continuum is unlikely to allow very good fits to the many molecular transitions simultaneously. It is therefore important in such cases to fit local continua around transitions where the nominal continuum is particularly uncertain. These local continua are shown in Figs. 1 and 2.

The reader will note that, for molecular transitions around which broad Lyman- $\alpha$  lines are also fitted, there will be strong degeneracies between the Lyman- $\alpha$  line parameters and those of the local continuum. For this reason, the local continua have polynomial degree of, at most, unity (i.e. they are either constants or straight lines in wavelength space). Also, the fitting code we use indicates cases where the degeneracies are so strong that a local continuum fit serves the same purpose as the Lyman- $\alpha$  line(s). It should be emphasised that these ambiguities and uncertainties in the local continuum shape all contribute to the uncertainties in the molecular line fits in a natural way because, in our  $\chi^2$  minimization process, all parameters of the fit are varied simultaneously. Most previous works (excluding, e.g., King et al. 2008) effectively determined fixed, local continua before fitting the molecular lines. This means that uncertainties in the continuum fits do not propagate through to the more interesting parameters of the subsequent fit, like  $\Delta\mu/\mu$ . While only a small effect, the uncertainty in  $\Delta\mu/\mu$  would be underestimated with such an approach.

Weak night sky emission is nominally subtracted during the initial flux extraction process, but systematic uncertainties in the zero flux level can and do remain. There are many obvious examples in Fig. 1 of saturated Lyman- $\alpha$  features which have non-zero average flux (either positive or, usually, negative) in their flat-bottomed line cores (e.g. features near 3107, 3137, 3171, 3317 and 3350 Å). We therefore included the zero level as a free parameter when fitting regions of spectrum which included nearly saturated absorption lines (either Lyman- $\alpha$  and/or molecular).

We add to our list of free parameters the oscillator strengths for the 10 H<sub>2</sub> transitions with  $J=0-3$  falling in the wavelength range  $\lambda_{\text{obs}} = 3345-3415 \text{ Å}$ . While establishing our fit, these transitions had noticeably higher optical depths than predicted by the model. For this reason the oscillator strengths for these transitions were left as free parameters to be determined in the  $\chi^2$  minimization process. Their fitted-to-calculated oscillator strength ratios,  $f_{\text{fit}}/f_{\text{calc}}$ , determined using our fiducial model (see below), range from 1.5 to 2.0. Although it is possible that the published oscillator strengths for these transitions, which (along with all other molecular lines used in our fit) are calculated rather than experimentally measured, are incorrect, we consider this very unlikely because these transitions are not affected by interference between multiple interacting H<sub>2</sub> states. Fits to H<sub>2</sub> transitions, which included some of these particular transitions, in other quasar absorbers also suggests their published oscillator strengths are reliable (J. King, private communication). An alternative explanation is motivated by the fact that these

transitions all fall on the combined O VI/Lyman- $\beta$  quasar emission line at  $\lambda_{\text{lab}} \approx 1025-1045 \text{ Å}$ : perhaps there is some inhomogeneity in the H<sub>2</sub> column density on the scale of the quasar broad emission-line region. Independent evidence for this scenario does not appear readily available in our spectrum, so it is difficult to confirm and will be explored in future work. Nevertheless, given this possible explanation, it is important to test whether these transitions affect our final results, and we conduct this consistency check in Section 4.1.

After establishing the best-fitting values of the model parameters described above, we introduce the last free parameter – the one of primary interest here –  $\Delta\mu/\mu$ . Note that only a single value of  $\Delta\mu/\mu$  describes all molecular transitions, including all their constituent VCs. Equation (1) states that a change in  $\mu$  manifests itself as a pattern of relative shifts between the different molecular transitions. Note that Fig. 3 shows that the diversity of  $K$  values ensures little covariance between  $\Delta\mu/\mu$  and other parameters; the pattern of shifts is not degenerate with, for example, the individual VC redshifts.

### 3.1.2 Minimizing $\chi^2$

The absorption model is constructed with the free parameters described above and the  $\chi^2$  between it and the spectral data is minimized using the program `VPFIT`<sup>4</sup>. This is a non-linear least-squares  $\chi^2$  minimization package written specifically for modelling complex, possibly interrelated absorption lines with a series of Voigt profiles. The model fit is convolved with an instrumental resolution function for comparison with the real spectrum; we used a Gaussian function with  $\text{FWHM} = 2.7 \text{ km s}^{-1}$  to match the resolution inferred from the extracted ThAr exposures. The software ‘understands’ that many molecular transitions can arise from the same  $J$ -level (i.e. that they have the same  $N$ ) and the ability to link physically related parameters, such as  $b$  and  $z_{\text{abs}}$  values, across many transitions is inherent in its design.

$\Delta\mu/\mu$  was recently added to the `VPFIT` code as a free parameter. The operation of a varying  $\mu$  on the molecular lines is functionally the same as the action of a varying  $\alpha$  on metal lines. That `VPFIT` returns the correct values of  $\Delta\alpha/\alpha$  and its uncertainty has been tested with a variety of simulations, including models with many strongly overlapping VCs which are, in some cases, blended with transitions from unrelated absorption clouds (Murphy et al. 2003). However, the fit we conduct here is substantially more complicated (though operationally similar) to such metal-line fits because the number of transitions and links between fitted parameters is much larger. Appendix A describes a Monte Carlo test of `VPFIT` using our actual fit to the molecular, Lyman- $\alpha$  forest and metal absorption lines in J2123–0050 as a synthetic spectrum, to which noise is added and into which a value of  $\Delta\mu/\mu = +5 \times 10^{-6}$  is inserted. The  $\chi^2$  minimization of the fit is then re-run on 420 such realizations. The mean and distribution of the  $\Delta\mu/\mu$  values recovered agrees well with expectations. We also conducted convergence tests using our fit to the real data to ensure that `VPFIT` arrived at the same value of  $\Delta\mu/\mu$  given a range of starting values; the default for all the results quoted in this paper was zero, but starting values of, e.g.,  $\pm 10$  and  $\pm 5 \times 10^{-6}$  gave the same results. The self-consistency checks conducted in Section 4 also corroborate the reliability of the algorithm.

The  $1-\sigma$  uncertainties on the best fitting parameters are derived by `VPFIT` from the appropriate diagonal terms of the final pa-

<sup>4</sup> <http://www.ast.cam.ac.uk/~rfc/vpfit.html>.



parameter covariance matrix. Given a particular absorption model, these errors represent only the formal statistical uncertainties derived from the flux error arrays of the fitted spectral regions. They do not reflect additional sources of error, like wavelength calibration uncertainties (see Section 4). Nor do they represent ‘model errors’ – the possible systematic errors involved with selecting an appropriate absorption model. We discuss the selection of the ‘best’ model at length in Section 3.2. `VPFIT` assumes that the fluxes (and flux errors) in neighbouring spectral pixels are uncorrelated. This is certainly not true in practice because the different quasar exposures were re-binned onto the same final wavelength grid for combination into a single spectrum. The correlation is reduced by averaging these exposures. And we are unable to detect the effect by comparing the RMS flux variations in unabsorbed regions with the final error spectrum; these values are very similar. We demonstrate in Section 4.2 that the binning of the different exposures onto the same wavelength grid produces a small systematic effect on  $\Delta\mu/\mu$ .

### 3.2 Fiducial absorption model

Nearly all the  $\text{H}_2$  and HD transitions detected in our spectrum of J2123–0050 were utilized in our fit; some transitions’ profiles were heavily blended with either nearby Lyman- $\alpha$  lines and/or suspected metal lines from one or more absorption systems (e.g. the LOP1  $\text{H}_2$  transition falling at  $\lambda_{\text{obs}} \approx 3396.2$ , see Fig. 1). No reliable fit could be obtained so we chose not to include these molecular lines in our sample.

In total, 86  $\text{H}_2$  transitions and 7 HD transitions are included in the fiducial fit. Only small regions around the molecular lines were fitted: each region contained only enough of the surrounding Lyman- $\alpha$  forest absorption to define the effective continuum against which the molecular lines were fitted. This meant that some molecular lines were fitted together in the same spectral region, joined by fitted Lyman- $\alpha$  forest lines and, in most cases, with a single (straight-line) local continuum and/or zero level. All the fitted regions are shown in Fig. 1. Assuming a simple, two VC model for the molecular absorption, an initial model of the Lyman- $\alpha$  forest lines, local continua and zero levels was established and refined. This same basic structure was used as a starting point in subsequent fits to determine the molecular velocity structure.

Although the absorption profiles in Fig. 2 clearly show two spectral features, it is possible, even likely, that the profiles comprise more than two VCs, each of which would be detectable (in the absence of the others) given the large number of molecular transitions we observe. The velocity structure best representing the molecular absorption profile was determined by fitting models with increasing numbers of molecular VCs and selecting the one with the smallest  $\chi^2$  per degree of freedom,  $\chi^2_\nu$ . This is one simple, standard method for discriminating between different models in  $\chi^2$  analyses, though other (very similar) ‘information criteria’ can also be used (e.g. Liddle 2007). Note that while (the minimum)  $\chi^2$  itself must always decrease when more free parameters are added to a model,  $\chi^2_\nu$  begins to *increase* when the additional parameters are not statistically justified. Figure 4 (lower panel) shows  $\chi^2_\nu$  versus the number of molecular VCs in the fit. The 4-component model has a lower  $\chi^2_\nu$  than the 3-component models and so is statistically preferred. 5- and 6-component fits were attempted but `VPFIT` found the additional components to be statistically unnecessary. That is, during the  $\chi^2$  minimization process those components became so weak that  $\chi^2$  became insensitive to their parameters, so the components were removed. Equivalently, if they had remained in the fit,

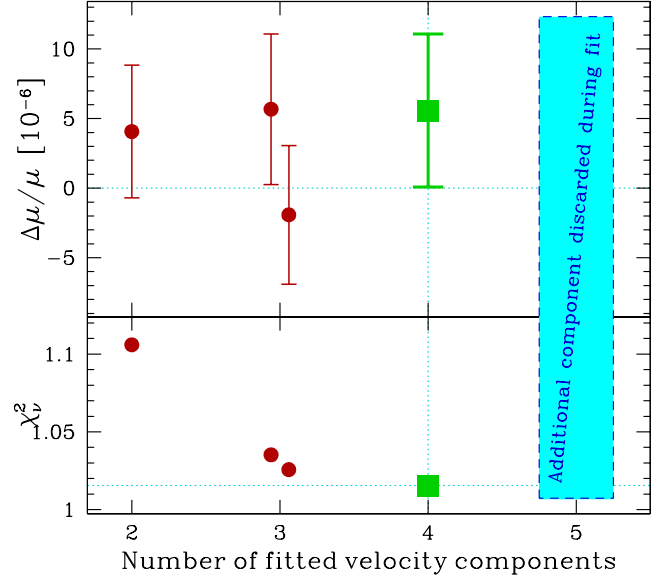


**Figure 4.**  $\Delta\mu/\mu$  (upper panel) and  $\chi^2$  per degree of freedom,  $\chi^2_\nu$  (lower panel), for different velocity structures characterised by the number of fitted absorption components. The 4-component fit, highlighted with square points, has the lowest  $\chi^2_\nu$  and is therefore the statistically preferred model. Two qualitatively different 3-component fits were possible; their results are horizontally offset here for clarity. Note the very different values of  $\Delta\mu/\mu$  they return, exemplifying the inherent systematic effects associated with ‘under-fitting’ the absorption profile. The error bars represent 1- $\sigma$  statistical uncertainties only; systematic errors are discussed in Section 4.2.

the final, reduced  $\chi^2_\nu$  would have been larger than for the fiducial 4-component fit.

Figures 1 and 2 show our fiducial 4-component fit. Table 3 provides the molecular cloud properties –  $z_{\text{abs}}$ ,  $b$  and the column densities in  $\text{H}_2$  and HD – and their formal 1- $\sigma$  statistical uncertainties in all relevant  $J$ -levels for each of the 4 VCs. Milutinovic et al. (in preparation) and Tumlinson et al. (in preparation) consider the absorption cloud properties in detail.

When visually assessing the fit in Figs. 1 and 2, one clearly cannot readily “see” 4 VCs and so one may worry that too many components are being fitted. However, this is merely a failing of the human eye to recognise coherent structures in almost 100 transitions simultaneously. For example, it is simple to simulate a similar molecular absorption profile as in the real data which comprises 4 components, one or more of which might be subtle enough to go unnoticed when visually assessing several transitions but which is statistically significant when  $\sim 100$  transitions are analysed properly. And so we must appeal to the objective, well-tested and well-understood model selection technique discussed above to *recover all the statistically significant structure in the line profiles*, otherwise we should expect systematic errors in our results. Previous works have demonstrated that ‘under-fitting’ – fitting too few VCs – causes strong systematic errors in quantities like  $\Delta\alpha/\alpha$  (Murphy, Webb & Flambaum 2008) and  $\Delta\mu/\mu$  (Murphy et al. 2008) when derived from individual absorption systems.

### 3.3 Fiducial result

Given an absorption model for which  $\chi^2$  has been minimized, determining  $\Delta\mu/\mu$  is straightforward: it is simply among the many



**Table 3.** Molecular absorption line parameters and  $1\text{-}\sigma$  statistical uncertainties for the 4-component fiducial fit in Figs. 1 and 2. Note the assumptions discussed in Section 3.1.1 which minimise the number of free parameters. In particular, the ratio of the HD ( $J = 0$ ) velocity component column densities to those of the corresponding  $\text{H}_2$   $J=0$  components is the same for all components. We also provide the total column density for each  $\text{H}_2$   $J$  level and for HD.

Com- ponent	$z_{\text{abs}}$	$b$ [km s $^{-1}$ ]	$J = 0$	$J = 1$	$\log N(\text{H}_2)$ [cm $^{-2}$ ]		$J = 4$	$J = 5$	$\log N(\text{HD})$ [cm $^{-2}$ ]
					$J = 2$	$J = 3$			
1	2.0593276(5)	$5.14 \pm 0.11$	$15.06 \pm 0.03$	$15.38 \pm 0.06$	$15.01 \pm 0.03$	$15.03 \pm 0.02$	$13.98 \pm 0.04$	$13.76 \pm 0.06$	$12.95 \pm 0.03$
2	2.0593290(4)	$1.92 \pm 0.06$	$15.80 \pm 0.40$	$17.52 \pm 0.04$	$16.23 \pm 0.16$	$15.16 \pm 0.25$	$13.45 \pm 0.09$	$12.78 \pm 0.37$	$13.69 \pm 0.05$
3	2.0595264(76)	$9.66 \pm 0.90$	$13.90 \pm 0.08$	$14.30 \pm 0.07$	$14.10 \pm 0.05$	$14.11 \pm 0.07$	$13.31 \pm 0.22$	$13.47 \pm 0.15$	
4	2.0595597(8)	$4.02 \pm 0.16$	$13.81 \pm 0.06$	$14.69 \pm 0.03$	$14.26 \pm 0.04$	$14.39 \pm 0.04$	$13.41 \pm 0.09$	$13.22 \pm 0.15$	
Total			$15.88 \pm 0.14$	$17.53 \pm 0.04$	$16.26 \pm 0.11$	$15.46 \pm 0.04$	$14.23 \pm 0.03$	$14.04 \pm 0.04$	$13.77 \pm 0.03$

free parameters determined in the  $\chi^2$  minimization process. For the 4-component fiducial model, we find that

$$\Delta\mu/\mu = (+5.6 \pm 5.5_{\text{stat}}) \times 10^{-6}. \quad (2)$$

Again, we emphasise that the  $1\text{-}\sigma$  uncertainty derives only from the spectrum’s photon statistics and is calculated from the relevant diagonal term of the final parameter covariance matrix. Given the range of  $K$  coefficients involved ( $\sim 0.05$ ; see Fig. 3), equation (1) implies that this uncertainty corresponds to a velocity precision of  $\sim 80 \text{ m s}^{-1}$ , or  $\sim 0.06$  spectral pixels.

Figure 4 (upper panel) shows the values of  $\Delta\mu/\mu$  for different models of the molecular velocity structure as characterised by the number of fitted absorption components. It graphically illustrates the dangers of ‘under-fitting’. The two different 3-component fits possible in this system give quite different  $\Delta\mu/\mu$  values. This large difference should be placed into the context that, since all fits were carried out on the same transitions in the same spectrum, the results from the different models are by no means independent; the statistical error bars are not the gauge of “significant” differences here. Also, the 2-component model may seem statistically acceptable at first since its  $\chi^2_\nu \sim 1$ . However, its  $\chi^2_\nu$  is much larger than for the 4-component fit and so it cannot be preferred in any objective sense. This is also true of the two different 3-component fits.

The inadequacies of 2- and 3-component fits are further exposed in Fig. 5. For the 24 relatively unblended  $\text{H}_2$  transitions, the residuals between the data and the model fit were normalized by the flux error arrays, shifted to a common velocity scale and averaged together. This forms a ‘composite residual spectrum’ as a diagnostic for under-fitting. By combining the residual structure between the model and the data for many transitions, we may now better appreciate “by eye” how well the model describes the statistically significant structure in those absorption profiles. Figure 5 clearly shows that the 2-component model fails to reproduce the real absorption profile shape, leaving many-pixel excursions outside the expected residual range as evidence of additional VCs. This is also true for the 3-component models. By comparison, the 4-component model leaves no obvious evidence for unmodelled, statistically significant structure.

## 4 INTERNAL CONSISTENCY AND SYSTEMATIC ERRORS

### 4.1 Consistency tests

The fiducial model in Section 3.2 includes all detected molecular transitions which could be fitted reliably; the data quality and degree of Lyman- $\alpha$  blending naturally weights each one’s contribution to  $\Delta\mu/\mu$ . The main advantage of this approach is objectivity:

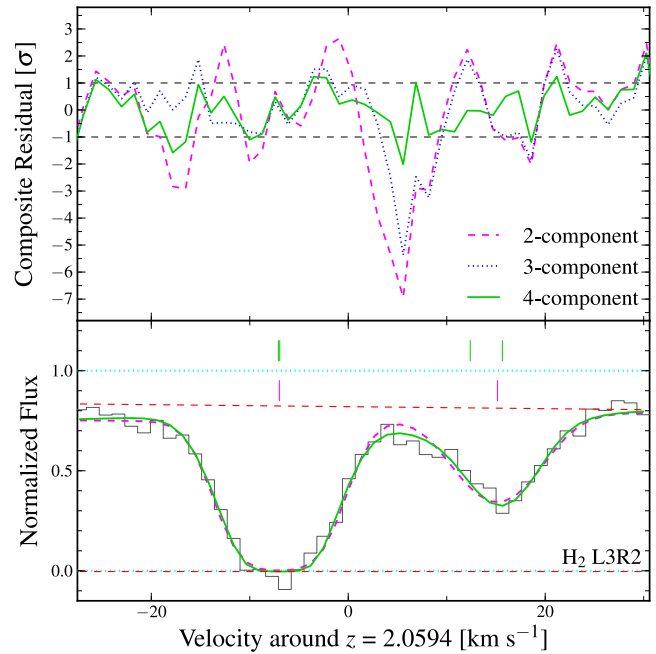


**Figure 5.** Composite residual spectra (CRS), formed from 24 relatively unblended  $\text{H}_2$  transitions. *Bottom panel:* An example  $\text{H}_2$  transition fitted with the 2- and fiducial 4-component models (dashed and solid curves, respectively). Only a small difference is noticeable by eye. However, the CRS panel above shows how significant the additional components are. *Upper panel:* CRS for the 4-component fiducial model (solid line) and the 2- and 3-component models (dashed and dotted lines, respectively; for clarity only one of the two possible 3-component models is shown here). Note the large, many-pixel excursions outside the  $\pm 1\text{-}\sigma$  range for the 2- and 3-component models, indicating unmodelled velocity structure. No such features exist for the 4-component model, as expected.

we do not select which transitions are ‘best’ to fit, or those which we expect, *a priori*, to provide the strongest constraints on  $\Delta\mu/\mu$ . Another approach is to fit only the ‘least blended’ or the ‘well-defined’ transitions. Deciding which transitions fit these descriptions is clearly subjective. Nevertheless, as a consistency check, we fitted spectral regions containing either no detectable Lyman- $\alpha$  blending or very simple and weak blending. We also excluded transitions blended with the Fe II lines described in Section 3.1.1. With 53  $\text{H}_2$  and 5 HD remaining transitions, a 4-component model was statistically preferred, returning  $\Delta\mu/\mu = (+5.0 \pm 5.9) \times 10^{-6}$ .

The  $J = 4$  and 5  $\text{H}_2$  transitions are weak, typically absorbing  $< 30\%$  of the local continuum. It is possible, though we would argue unlikely, that unmodelled structure in the nearby Lyman- $\alpha$

forest lines and/or local continua for these transitions will have a greater relative effect on the molecular profile fits in these cases. A 4-component fit where the 28  $J = 4$  and 5 transitions are prevented from directly influencing  $\Delta\mu/\mu$ , effectively by setting their  $K$  values to zero<sup>5</sup>, yielded  $\Delta\mu/\mu = (+4.8 \pm 5.6) \times 10^{-6}$ . The very small increase in the statistical uncertainty compared to equation (2) is symptomatic of how weakly these  $J = 4$  and 5 transitions affect  $\Delta\mu/\mu$ , due primarily to their low optical depth. A similar problem may exist for the HD transitions, which are also very weak; a 4-component model with the HD transitions' dependence on  $\mu$  removed returned  $\Delta\mu/\mu = (+4.1 \pm 5.8) \times 10^{-6}$ .

In Section 3.1.1 we described how the predicted optical depths for the  $J=0-3$   $\text{H}_2$  transitions falling at  $\lambda_{\text{obs}} = 3345-3415 \text{ \AA}$  (i.e. where the Lyman- $\beta/\text{O IV}$  quasar emission line falls) were too low, possibly because there is some inhomogeneity in the  $\text{H}_2$  column density on the angular scale of the quasar broad line region. We therefore allowed these transitions' oscillator strengths to effectively vary as free parameters in the fit. This may not be an accurate parametrisation so we must assess the extent to which it affects our conclusions. Firstly, if we remove the  $\mu$ -dependence of the 10  $J=0-3$   $\text{H}_2$  transitions concerned (by setting their  $K$  values to zero), a 4-component fit gives  $\Delta\mu/\mu = (+7.0 \pm 6.7) \times 10^{-6}$ . Another test is to fit all  $\text{H}_2/\text{HD}$  transitions with oscillator strengths as free parameters, i.e. the column densities of different transitions from the same  $J$ -level are allowed to be different, as in the fits conducted by King et al. (2008). A 4-component fit yields  $\Delta\mu/\mu = (+5.4 \pm 5.5) \times 10^{-6}$ . Notice that the statistical uncertainty does not increase discernibly here, even though the number of fitted parameters has been increased significantly; this is because the many column-density parameters for the molecular velocity components of each transition have very little influence on the fitted line positions, which is what primarily affects  $\Delta\mu/\mu$ .

Our fiducial model assumes that a given molecular VC has the same  $b$ -parameter in all  $J$ -levels. One can envisage different physical effects which may invalidate this model assumption. And while we do not find obvious evidence to the contrary in our spectra, it may be that our fitting approach – where we make the assumption and then build up the fit to the molecular lines by adding VCs until all the statistical structure in the molecular line profiles is modelled – is not the best method for identifying such an effect. We have therefore relaxed the assumption to test its effect on the fitted value of  $\Delta\mu/\mu$ : when allowing VCs to have different  $b$ -parameters in different  $J$ -levels,  $\Delta\mu/\mu = (+7.9 \pm 5.6) \times 10^{-6}$ . While there is small change in the value of  $\Delta\mu/\mu$  with respect to the fiducial value in equation (2), it does not represent a strong model dependency. We note in passing that allowing VCs to have different  $b$ -parameters in different  $J$ -levels does not solve the problem, discussed above, of some  $\text{H}_2$  transitions appearing stronger in the spectrum compared to the prediction of the fiducial fit; those transitions come from a range of different  $J$ -levels.

Finally, `vffit` allows different values of  $\Delta\mu/\mu$  to be fitted for the different  $\text{H}_2$   $J$ -levels. In this test we maintain the assumption that all  $J$ -levels have the same velocity structure, i.e. all  $J$ -levels are

<sup>5</sup> At first it may seem that a simpler, more easily interpretable alternative would be to completely remove the  $J=4$  and 5 (or HD) transitions to test their influence on the fiducial result. However, as we describe in Section 3.1.1 and as is apparent in Fig. 1, several molecular transitions are often fitted together in one contiguous fitting region. This is because different transitions can be blended together, or be effectively joined by the same Lyman- $\alpha$  forest lines. Thus, in principle, removing individual molecular transitions from the fit is not possible without removing entire fitting regions.

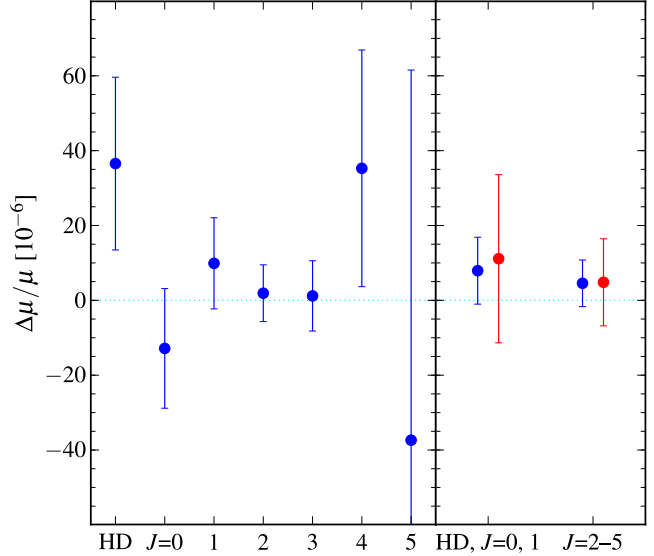


**Figure 6.** *Left panel:*  $\Delta\mu/\mu$  for each  $\text{H}_2$   $J$ -level and HD, assuming they all have the same 4-component velocity structure. *Right panel:*  $\Delta\mu/\mu$  for two groups of transitions, HD plus  $\text{H}_2$   $J=0-1$  and  $\text{H}_2$   $J=2-5$ . The dark/blue points derive from a model assuming the same velocity structure in both groups, whereas the light/red points (offset to the right for clarity) allow the velocity structure for the two groups to differ. Both groups were fitted with a 4-component model in both cases.

fitted with 4 VCs, with each VC having the same redshift in all transitions (we relax this assumption in Section 4.2). We also derived a separate value from the HD lines. The resulting values of  $\Delta\mu/\mu$  are plotted in Fig. 6 (left panel). This plot is useful in clarifying the relative contributions the series of transitions from different  $\text{H}_2$   $J$ -levels and HD make to the final uncertainty on  $\Delta\mu/\mu$ . Of course, the velocity structure was assumed to be the same in all cases, so the different  $\Delta\mu/\mu$  values are not strictly independent. Nevertheless, we note general agreement, especially for the  $\text{H}_2$   $J=1-3$  transitions. Since the error bars are relatively large for the other  $J$ -levels and HD, we also derived less uncertain values by grouping the HD and  $\text{H}_2$   $J=0-1$  transitions together. A similar grouping of the  $\text{H}_2$   $J=2-5$  transitions gave a similar value of  $\Delta\mu/\mu$ . These values are plotted on Fig. 6 (right panel).

The above consistency checks indicate that the fiducial value of  $\Delta\mu/\mu$  is not strongly dependent on the assumptions made in our 4-component fit. Individually relaxing these assumptions produces little change in the measured value of  $\Delta\mu/\mu$ . This is also consistent with there being no important problems with our data, or our analysis.

## 4.2 Systematic errors

### 4.2.1 Specific, known wavelength calibration errors

Since a varying  $\mu$  should cause velocity shifts between molecular transitions, wavelength calibration errors which *distort* the wavelength scale are clearly important potential sources of systematic errors in  $\Delta\mu/\mu$ . Note that, as implied by equation (1), effects which shift the wavelength scale by a constant velocity at all wavelengths are generally unimportant<sup>6</sup>. The first, most obvious possibility is

<sup>6</sup> This is not strictly true when many quasar exposures are combined, as is the case here. If different velocity shifts are applied to the different quasar

that the wavelength scale of the ThAr exposures was incorrectly determined. This is easily checked. The wavelength calibration residuals, with RMS  $\sim 80 \text{ m s}^{-1}$ , are consistent with being symmetrically distributed around the final wavelength solution at all wavelengths. Because many  $\text{H}_2/\text{HD}$  transitions are used, with a range of wavelengths, this reduces the overall calibration error substantially. For example, over the 12 HIRES echelle orders covering the wavelength range where the molecular lines fall (3071–3421 Å), 150–200 ThAr lines are used to calibrate our ThAr exposures. Clearly though, systematic trends in these residuals are still possible. Using the same technique employed in Murphy et al. (2007) to track systematic patterns in the ThAr calibration residuals, the possible distortion in the wavelength scale between 3070 and 3430 Å is  $<30 \text{ m s}^{-1}$ . This corresponds to a systematic error in  $\Delta\mu/\mu$  of  $\pm 2.0 \times 10^{-6}$  at most.

Once determined from the ThAr exposures, the wavelength solutions are simply applied to the corresponding quasar exposures. Drifts in the refractive index of air inside HIRES between the ThAr and quasar exposures will therefore cause miscalibrations. The temperature and atmospheric pressure drifts during our observations were  $<1 \text{ K}$  and  $<1 \text{ mbar}$  respectively. According to the Edlen (1966) formula for the refractive index of air, this would cause *differential* velocity shifts between 3070 and 3430 Å of  $<10 \text{ m s}^{-1}$ , which are negligible.

The quasar and ThAr light traverse similar but not identical paths through HIRES. Only the quasar light passes from the telescope into HIRES and the ThAr light (nearly) uniformly illuminates the slit while the quasar light is centrally concentrated. *Differential* distortions of the wavelength scale – within individual echelle orders (‘intra-order’) and over longer wavelength ranges (‘long-range’) – may therefore occur in the quasar and corresponding ThAr exposures.

Griest et al. (2010) recently identified intra-order distortions in HIRES. They compared the wavelength scales established using ThAr exposures with those imprinted on quasar exposures by an iodine absorption cell. The distortions are such that, for different transitions at the same redshift in a quasar spectrum, those at the order edges appear at positive velocities with respect to transitions at the order centres when calibrated with a ThAr exposure. The peak-to-peak velocity distortion is  $\sim 500 \text{ m s}^{-1}$  at  $\sim 5600 \text{ Å}$  and may worsen (improve) with increasing (decreasing) wavelength; see figure 4 of Griest et al. (2010). The effect is similar (though not identical) for all echelle orders in the wavelength range  $\sim 5000$ – $6200 \text{ Å}$  covered by the iodine cell absorption. If we assume that similar intra-order distortions apply to our spectra of J2123–0050 at much bluer wavelengths then, because the molecular transitions of interest lie at different positions along different echelle orders, we should expect the effect on  $\Delta\mu/\mu$  to be suppressed. To illustrate this, a very crude estimate of the ‘residual’ velocity distortion is just the observed  $\sim 500 \text{ m s}^{-1}$  peak-to-peak intra-order value reduced according to the number of molecular transitions observed, i.e.  $\sim 500 \text{ m s}^{-1} / \sqrt{93} \approx 52 \text{ m s}^{-1}$ . This corresponds to a systematic error in  $\Delta\mu/\mu$  of approximately  $\pm 3.5 \times 10^{-6}$ .

This crude calculation fails to take into account the strong variation in the spectral SNR across the wavelength range containing the  $\text{H}_2/\text{HD}$  transitions, their different sensitivities to  $\mu$  variation, where they fall with respect to echelle order edges in our particu-

lar spectrum and other factors such as the degree of blending with Lyman- $\alpha$  forest lines of each molecular transition. A simple Monte Carlo simulation which takes into account the first two of these effects – SNR and  $K$  for each transition – was undertaken as follows. Each realisation comprised a velocity shift,  $\Delta v_i$ , chosen randomly for each transition,  $i$ , from the  $500 \text{ m s}^{-1}$  peak-to-peak interval spanned by the intra-order distortions identified by Griest et al. (2010). The square of the SNR of the spectral data surrounding the molecular transitions then weighted a linear least squares fit of the  $\Delta v_i/c$  versus  $K$  values, the slope of which provided a value of  $\Delta\mu/\mu$  for that realisation – see equation (1). The distribution of values for  $\Delta\mu/\mu$  over hundreds of thousands of Monte Carlo realizations was close to Gaussian with an RMS of  $4.8 \times 10^{-6}$ .

However, the most direct calculation of the possible systematic effect on  $\Delta\mu/\mu$ , which takes into account all remaining effects (e.g. positions of transitions with respect to order edges, line blending etc.), can be obtained by attempting to remove the intra-order distortions from our individual quasar exposures. To this end we applied a  $-250 \text{ m s}^{-1}$  velocity shift to the wavelengths of all echelle order centres for all our quasar exposures. The shift was reduced linearly with distance from the order centres to reach  $+250 \text{ m s}^{-1}$  at the order edges. The spectra were recombined again to form a final 1-dimensional spectrum to which we fit the 4-component model as before. The value of  $\Delta\mu/\mu$  derived from this ‘corrected’ spectrum was  $(+3.7 \pm 5.5) \times 10^{-6}$ . Compared with the fiducial 4-component result of  $(+5.6 \pm 5.3) \times 10^{-6}$ , this represents a smaller effect, approximately  $\pm 1.9 \times 10^{-6}$ , than expected from the cruder estimates above. Given that Griest et al. (2010) observed smaller distortions at shorter wavelengths, it may also overestimate the real effect.

To summarise the above considerations, if the intra-order distortions of the wavelength scale identified by Griest et al. (2010) at  $5000$ – $6500 \text{ Å}$  also affect the much bluer wavelengths of interest here, the implied systematic error on  $\Delta\mu/\mu$  is approximately  $\pm 1.9 \times 10^{-6}$  in our particular spectrum. However, the main assumption in this estimate is that we have modelled the Griest et al. intra-order distortions reliably. The physical explanation for those distortions is not yet known, so we do not know whether, for example, the phase of the saw-tooth distortion pattern with respect to the order edges is the same for all quasar exposures taken at different times and with different telescope and observational conditions (e.g. telescope pointing direction, seeing etc.), nor do we know whether the intra-order distortions follow a general saw-tooth pattern at all, or if the distortions in the UV can be predicted based on those in the iodine cell’s calibration range. These important questions should be resolved with future observations and careful re-calibrations of HIRES. Thus, our estimate of  $\pm 1.9 \times 10^{-6}$  for the systematic error due to intra-order distortions may also be subject to model errors.

#### 4.2.2 General, unknown wavelength calibration errors

In Fig. 3 one observes a general decrease in the  $K$  coefficients for the fitted Lyman  $\text{H}_2$  transitions with increasing wavelength. A long range, monotonic distortion of the wavelength scale is therefore nearly degenerate (though not completely) with the effect of a shift in  $\mu$  on the Lyman lines. Put another way, a systematic effect which produced a long-range wavelength distortion would cause a strong systematic effect on  $\Delta\mu/\mu$  if only the Lyman  $\text{H}_2$  transitions were fitted. It is therefore important to fit the Werner transitions as well: their  $K$  values are very different to those of the Lyman transitions at similar wavelengths, potentially breaking the degeneracy between  $\Delta\mu/\mu$  and long-range wavelength distortions and improving resistance to systematic errors. If we remove the  $\mu$ -dependence of the

exposures, and if the relative weights of the exposures vary with wavelength when forming the final, combined spectrum, then small relative velocity shifts will be measured between transitions at different wavelengths.

12 H<sub>2</sub> and 1 HD Werner transitions in our fit, a 4-component model is statistically preferred and returns  $\Delta\mu/\mu = (+5.2 \pm 5.6) \times 10^{-6}$ , very similar to the fiducial result in equation (2).

However, the SNR at bluer wavelengths where the Werner transitions fall is much lower than for the reddest Lyman transitions, so the effect of the Werner transitions in breaking this degeneracy between  $\Delta\mu/\mu$  and long-range wavelength distortions is reduced. To illustrate this we inserted such a distortion into a simulated version of our spectrum. The wavelength scale for one of the Monte Carlo realizations from Appendix A was compressed according to

$$\frac{\Delta v_j}{c} = \left( \frac{\Delta\mu}{\mu} \right)_{\text{sys}} (a\lambda_j + b), \quad (3)$$

where  $\lambda_j$  is the initial (observed) wavelength of a given pixel,  $\Delta v_j$  is the velocity shift applied to it,  $(\Delta\mu/\mu)_{\text{sys}}$  is the systematic error in  $\Delta\mu/\mu$  we seek to mimic, and the constants  $a$  and  $b$  are set to mimic the general decrease in  $K$  with increasing wavelength for the Lyman transitions (see Fig. 3). To obtain a spurious shift in  $\Delta\mu/\mu$  of approximately  $+15 \times 10^{-6}$ , we set  $(\Delta\mu/\mu)_{\text{sys}} = 15 \times 10^{-6}$ ,  $a = -1.3 \times 10^{-4} \text{ \AA}^{-1}$  and  $b = 0.4345$ . Indeed, when this spectrum is fitted with the fiducial model used to generate it,  $\Delta\mu/\mu$  shifts from  $4.0 \times 10^{-6}$  before compression to  $16.2 \times 10^{-6}$  after compression, as expected. And when the  $\mu$ -dependence of the 12 H<sub>2</sub> and 1 HD Werner transitions is removed when fitting the compressed spectrum,  $\Delta\mu/\mu$  only changes by small amount to  $17.3 \times 10^{-6}$ . That is, simply removing the Werner transitions' dependence on  $\mu$  is not a very effective test for long-range distortions of the wavelength scale.

A more meaningful test is to fit only the Lyman and Werner transitions in the bluest part of the spectrum and not the redder Lyman transitions. If we fit the 51 Werner and Lyman lines bluewards of  $\lambda_{\text{obs}} = 3230 \text{ \AA}$  in our simulated spectrum,  $\Delta\mu/\mu$  only shifts from 6.1 to  $7.4 \times 10^{-6}$  when the compression is introduced, indicating the expected resistance to this systematic error. With the  $\mu$ -dependence of the 12 H<sub>2</sub> and 1 HD Werner transitions removed in this fit,  $\Delta\mu/\mu$  is 7.6 and  $11.3 \times 10^{-6}$  before and after compression, respectively. That is, if there is a long-range, monotonic distortion of the wavelength scale, we expect to find a substantial shift in  $\Delta\mu/\mu$  when the  $\mu$ -dependence of the Werner transitions is removed. For the real spectrum, the value of  $\Delta\mu/\mu$  derived from the Lyman and Werner lines bluewards of  $\lambda_{\text{obs}} = 3230 \text{ \AA}$  is  $(+12.1 \pm 11.7) \times 10^{-6}$  and, when the  $\mu$ -dependence of the Werner transitions is removed, this changes to  $(+12.8 \pm 14.3) \times 10^{-6}$ . Thus, despite this being a reasonable test for long-range distortions of the wavelength scale, it fails to reveal evidence for such an effect in our spectrum of J1213–0050.

#### 4.2.3 Errors from spectral re-dispersion

As discussed in Section 2.1, the spectrum to which we fit our absorption profile models is the weighted mean of several individual quasar exposures. In combining these spectra, they were all re-dispersed onto the same wavelength grid. Note that the data reduction procedures we employed meant that each exposure was only re-binned in this way just once. Nevertheless, this rebinning introduces correlations between the flux (and flux uncertainty) of neighbouring pixels. In principle, this should have a small effect on the fitted centroid of any spectral feature and so, even though we fit many molecular lines simultaneously, a residual effect on  $\Delta\mu/\mu$  may exist. To test the possible size of this effect we re-combined the quasar exposures onto a variety of slightly different wavelength

grids with different dispersions (i.e.  $\text{km s}^{-1}$  per pixel) and wavelength zero points. The values of  $\Delta\mu/\mu$  derived from these different versions of the final combined spectrum varied by  $\pm 0.8 \times 10^{-6}$  at most.

#### 4.2.4 Velocity structure

The fiducial absorption model assumes that the molecular velocity structure is the same in all  $J$ -levels (see Section 3.1.1). In a Galactic line of sight with H<sub>2</sub> absorption, Jenkins & Peimbert (1997) found that (part of) the absorption profile becomes broader and systematically shifts in velocity with increasing  $J$ . The absorption profiles comprise many velocity components spanning velocities greater than the broadening and shifting observed. This is consistent with the velocity structure being the same in all  $J$ -levels where some constituent VCs have low optical depths in the low- $J$  transitions but are relatively strong in the higher- $J$  transitions. Thus, if one knew the velocity structure – or one used as many VCs as required to model all the statistically significant structure in the observed line profiles – one may not necessarily find that individual VCs broaden or shift with increasing  $J$ . Instead, one would simply find that the relative column densities of neighbouring VCs changed with increasing  $J$ . However, if any significant unmodelled structure remains, and its effective optical depth varies as a function of  $J$ , it may cause a systematic effect in  $\Delta\mu/\mu$ . An example of this effect in an H<sub>2</sub>-bearing quasar absorber was identified by Noterdaeme et al. (2007).

Ivanchik et al. (2005) considered this possibility, pointing out that the potential effect on  $\Delta\mu/\mu$  is diminished because transitions of different  $J$  are interspersed in wavelength space. This is also evident in Fig. 3 (lower panel). Although we emphasise that Figs. 4 and 5 demonstrate that all the statistically significant structure in the molecular transitions has been modelled, we can make a direct test for this effect by allowing  $\Delta\mu/\mu$  and the velocity structure to be different for different H<sub>2</sub>  $J$ -levels and HD. In Section 4.1 we made only the former assumption and found that a stringent test, with relatively small statistical uncertainties, was only possible when grouping together different H<sub>2</sub>  $J$ -levels and HD. By introducing more free parameters in this new test – the different VC redshifts – for different H<sub>2</sub>  $J$ -levels and HD (or groups thereof), we expect even larger uncertainties. So we again form groups of H<sub>2</sub>  $J$ -levels and HD, deriving a single value of  $\Delta\mu/\mu$  with a 4-component velocity structure in the HD and H<sub>2</sub>  $J=0-1$  levels and another value with a different 4-component model for the H<sub>2</sub>  $J=2-5$  levels. The two values are shown in Fig. 6 (right panel): we see no strong evidence for the effects of unmodelled velocity structure as a function of species (H<sub>2</sub>  $J$ -level or HD).

#### 4.2.5 Summary of systematic errors

To summarise the above discussion, by far the two most important potential systematic effects are small distortions in the ThAr wavelength scale and intra-order distortions of the quasar wavelength scale relative to the ThAr exposures. These contribute systematic errors in  $\Delta\mu/\mu$  of approximately  $\pm 2.0$  and  $\pm 1.9 \times 10^{-6}$ , respectively. Effects from re-dispersion of the spectra may contribute as much as  $\pm 0.8 \times 10^{-6}$ .



## 5 SUMMARY AND DISCUSSION

Our final result for the  $z_{\text{abs}} = 2.059$  absorber observed in the Keck spectrum of J2123–0050 is

$$\Delta\mu/\mu = (+5.6 \pm 5.5_{\text{stat}} \pm 2.9_{\text{sys}}) \times 10^{-6}. \quad (4)$$

This includes the  $1\text{-}\sigma$  statistical error [see equation (2)] and the quadrature addition of the three main potential systematic errors discussed in Section 4.2: long- and short-range wavelength calibration errors and effects from re-dispersion of the spectra. It is difficult to estimate the confidence level represented by the quoted systematic error component, though it is likely to represent a higher confidence (i.e.  $>68$  per cent) than the  $1\text{-}\sigma$  level represented by the quoted statistical uncertainty. However, we emphasise that the systematic error estimate for short-range calibration errors is based only on the limited information about intra-order wavelength distortions currently accessible (Griest et al. 2010); it is therefore model-dependent and may under- or over-estimate the true effect, if present.

Our result in equation (4) is based on fitting an absorption profile model to particular regions of the spectrum which contain 86  $\text{H}_2$  and 7 HD transitions, most of which are blended to varying extents with broader Lyman- $\alpha$  forest lines, and a few of which blend with well-constrained, weak metal absorption. All these lines, together with local continua and zero flux level adjustments for most lines, are fitted simultaneously to determine a single, best-fit value of  $\Delta\mu/\mu$ . To reduce the number of free parameters in the fit, two main physically motivated assumptions were made about the molecular transitions: that the velocity structure is the same for all  $J$ -levels and that individual velocity components have the same Doppler broadening parameter in all  $J$ -levels. Also, since the HD lines are so weak, it was convenient to assume that the HD ( $J = 0$ ) velocity components follow the same relative optical depth pattern as the  $\text{H}_2$   $J = 0$  transitions. Finally, the oscillator strengths of some  $\text{H}_2$  transitions were effectively treated as free parameters because their optical depths are higher than expected based on our fiducial model; see Section 3.1.1. However, we have individually relaxed each of these assumptions and/or removed the transitions they pertain to, and find the fiducial result in equation (4) to be quite insensitive to them.

Figure 7 compares the contemporary astronomical  $\Delta\mu/\mu$  constraints outside our Galaxy. Our new constraint is the first from Keck with precision comparable to those from the VLT. Agreement is seen between our Keck result and the three VLT constraints from King et al. (2008) who used similar calibration and fitting techniques to those described here. Such consistency is encouraging, allowing us to (at least formally) derive a weighted mean<sup>7</sup> value of  $\Delta\mu/\mu = (+3.5 \pm 2.8) \times 10^{-6}$  for redshifts  $z = 2.0\text{--}3.1$ . Statistical errors are shown as thinner error bars with shorter terminators in Fig. 7. Although the statistical error in our new measurement is slightly smaller than for two of the King et al. (2008) absorbers, it is slightly worse than for the  $z_{\text{abs}} = 2.811$  absorber towards Q 0528–250, i.e.  $3.9 \times 10^{-6}$ . The main reason for this is the lower SNR of our current Keck spectrum of J2123–0050, despite the fact that its spectral resolution is higher and more molecular transitions were utilized in our analysis. Since J2123–0050 is relatively bright, improvements in both the statistical and systematic uncertainties can be achieved with new observations of moderate duration. And

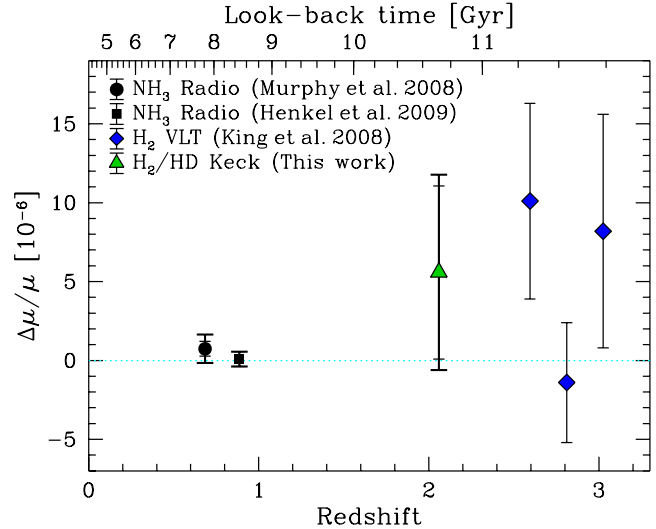


**Figure 7.** Current extragalactic  $\Delta\mu/\mu$  constraints. The legend gives the reference for each point and the method used, i.e.  $\text{H}_2$  or  $\text{NH}_3$  quasar absorption lines.  $1\text{-}\sigma$  statistical uncertainties are indicated with thinner error bars with shorter terminators while the thicker error bars with longer terminators show the systematic error added in quadrature with the statistical ones. Diamonds represent the VLT constraints; our new measurement is the only one from Keck. Note that two of the King et al. (2008) absorbers use the same raw VLT data as those analysed previously by Ivanchik et al. (2005) and Reinhold et al. (2006). We omit the results of those two studies assuming that the improved analysis in King et al. has yielded more reliable results. For clarity, we also omit the other recent re-analyses of the same two absorbers by Wendt & Reimers (2008) and Thompson et al. (2009); these works also yielded null results with somewhat larger errors than reported by King et al.

since it is located near the celestial equator, J2123–0050 can easily be observed from both Keck and VLT, enabling a further opportunity to check for instrumental systematic errors. We have recently undertaken such observations and a future paper will report the results.

At  $z < 1$ , comparison of the radio inversion transitions of  $\text{NH}_3$  – which have enhanced sensitivity to  $\mu$ -variation (van Veldhoven et al. 2004; Flambaum & Kozlov 2007) – with less sensitive molecular rotational lines (e.g.  $\text{HCO}^+$ ,  $\text{HCN}$ ), has yielded two very strong constraints,  $\Delta\mu/\mu = (+0.74 \pm 0.47_{\text{stat}} \pm 0.76_{\text{sys}}) \times 10^{-6}$  at  $z = 0.685$  (Murphy et al. 2008) and  $(+0.08 \pm 0.47_{\text{sys}}) \times 10^{-6}$  at  $z = 0.889$  (Henkel et al. 2009). These results are plotted in Fig. 7 for comparison with the higher redshift  $\text{H}_2/\text{HD}$  constraints. It is clear that the radio constraints have superior precision and, by current estimates, smaller potential systematic errors. However, direct comparison of the radio and optical constraints is difficult because of the possibility, in principle, for spatial variations in  $\mu$ : the different molecular species ( $\text{NH}_3$  and  $\text{H}_2/\text{HD}$ ) trace regions of different densities and, therefore, different spatial scales and environment. If  $\mu$  does vary, we do not know what that variation depends on, so it is presumptuous to prefer one type of measurement over the other. Indeed, this is highlighted by Levshakov et al. (2008) who studied  $\text{NH}_3$  inversion *emission* lines from numerous Galactic molecular clouds. With statistical errors from previous literature of  $\sim 0.1 \text{ km s}^{-1}$  they find velocity offsets between the  $\text{NH}_3$  inversion and rotational molecular emission of up to  $|\Delta v| \sim 0.5 \text{ km s}^{-1}$  in individual systems. This might indicate spatial variations in  $\mu$  throughout our Galaxy, although intrinsic shifts between emission lines of different molecules are to be expected. The possibility for

<sup>7</sup> We added the statistical and systematic error components on our new result in quadrature for this calculation. No systematic error estimates are available for the King et al. results.

both space- and time-variations in  $\mu$  is even more important given the different redshift ranges currently probed by the radio and optical constraints.

Several other quasar absorption- and emission-line techniques for constraining variations in combinations of fundamental constants involving  $\mu$  are also of note. For example, comparison of H I 21-cm absorption with metal absorption lines constrains the quantity  $X \equiv g_p \alpha^2 / \mu$  where  $g_p$  is the proton  $g$ -factor. A variety of analyses using different metal-ions have been performed (e.g. Wolfe et al. 1976; Tzanavaris et al. 2005; Kanekar et al. 2006), with measurements from 9 absorption systems at  $0.23 < z_{\text{abs}} < 2.35$  by Tzanavaris et al. (2007) providing a constraint of  $\Delta X/X = (+6.3 \pm 9.9) \times 10^{-6}$ . However, the fact that the H I 21-cm and metal-line velocity structures are observationally dissimilar – probably because the radio morphology of most background quasars is not point-like – means that improvements must come by averaging over many sight-lines and/or carefully selecting quasars with point-like radio morphologies. Comparing H I 21-cm with the ‘main’ OH 18-cm absorption lines, which constrains  $F \equiv g_p (\mu \alpha^2)^{1.57}$  (Chengalur & Kanekar 2003), suffers less from this problem because of the similarity of the wavelengths concerned. Kanekar et al. (2005) analysed two absorbers at  $z_{\text{abs}} = 0.685$  and  $0.765$  to obtain the constraint  $\Delta F/F = (+4.4 \pm 3.6_{\text{stat}} \pm 10_{\text{sys}}) \times 10^{-6}$ . Finally, a promising technique is to use the ‘satellite’ OH 18-cm lines which, when the ground state level populations are inverted, results in the two transitions being ‘conjugate’ – one occurs in emission, the other in absorption, but they have the same optical depth profile and are guaranteed to arise in the same gas clouds. Comparing the sum and difference of the optical depth profiles of the 1612 and 1720 MHz conjugate satellite lines constrains  $G \equiv g_p (\mu \alpha^2)^{1.85}$  (Chengalur & Kanekar 2003). With only two such systems known outside our Galaxy, and with their published spectra having very low SNR, no definitive constraints on  $\Delta G/G$  yet exist (Darling 2004; Kanekar et al. 2005). Kanekar (2008) has presented a preliminary constraint of  $|\Delta G/G| < 11 \times 10^{-6}$  for a system at  $z = 0.247$  and also  $< 12 \times 10^{-6}$  for a Galactic system, Centaurus A.

While these constraints on variations in  $X$ ,  $F$  and  $G$  are important in their own right, it is difficult to compare them with constraints on  $\Delta\mu/\mu$ . As we mentioned in Section 1, predictions for the relationships between variations in, e.g.,  $\mu$  and  $\alpha$  are strongly model-dependent (Dent et al. 2008). Currently, there is also no overlap with the redshift range occupied by the H<sub>2</sub>/HD constraints on  $\Delta\mu/\mu$  and variations in  $X$ ,  $F$  and/or  $G$ .

A striking feature of Fig. 7 is the paucity of direct  $\mu$  measurements outside our Galaxy. Compare this with, for example, the 143 constraints on  $\alpha$ -variation available from Keck/HIRES over the redshift range  $z = 0.2\text{--}4.2$  (Murphy et al. 2004). Clearly, much larger samples of both NH<sub>3</sub> and H<sub>2</sub>/HD constraints, in overlapping redshift ranges, would allow additional tests for systematic errors and stronger conclusions to be drawn. In this respect it is important to reduce the statistical errors in individual H<sub>2</sub>/HD measurements. This can only be done by substantially increasing the SNR of the optical spectra. We have demonstrated here that, at least for the Keck/HIRES spectrum of J2123–0050, the statistical error still dominates over systematic errors [equation (4)]. Nevertheless, if such systematic errors are not also reduced by improving the spectral SNR, it becomes more important to greatly increase the number of H<sub>2</sub>/HD absorbers for measuring  $\Delta\mu/\mu$  in order to approach the precision demonstrated in the NH<sub>3</sub> measurements. Surveys targeting particularly gas- and/or metal-rich absorbers have been successful in discovering more H<sub>2</sub>/HD systems (e.g. Ledoux et al. 2003; Petitjean et al. 2006; Noterdaeme et al. 2008). The large number of

damped Lyman- $\alpha$  systems identified in the Sloan Digital Sky Survey (e.g. Prochaska & Wolfe 2009) offers a new avenue for discovery, J2123–0050 being one such example. Of course, finding more NH<sub>3</sub> absorbers, particularly at  $z > 1$  would be highly desirable as well.

## ACKNOWLEDGMENTS

The data presented herein were obtained at the W. M. Keck Observatory, which is operated as a scientific partnership among the California Institute of Technology, the University of California and the National Aeronautics and Space Administration. The Observatory was made possible by the generous financial support of the W. M. Keck Foundation. The authors wish to recognise and acknowledge the very significant cultural role and reverence that the summit of Mauna Kea has always had within the indigenous Hawaiian community. We are most fortunate to have the opportunity to conduct observations from this mountain. We thank the anonymous referee for their measured and insightful review and for helping us improve the manuscript. MTM thanks the Australian Research Council for a QEII Research Fellowship (DP0877998). JXP is supported by NSF grants AST-0709235 and AST-0548180. WU acknowledges financial support from the Netherlands Foundation for Fundamental Research of Matter (FOM).

## REFERENCES

- Abgrall H., Roueff E., 2006, *A&A*, 445, 361
- Abgrall H., Roueff E., Drira I., 2000, *A&AS*, 141, 297
- Abgrall H., Roueff E., Launay F., Roncin J.-Y., 1994, *Canadian J. Phys.*, 72, 856
- Abgrall H., Roueff E., Launay F., Roncin J.Y., Subtil J.L., 1993, *J. Molecular Spectrosc.*, 157, 512
- Bahcall J.N., Sargent W.L.W., Schmidt M., 1967, *ApJ*, 149, L11
- Bailey D., Salumbides E.J., Vervloet M., Ubachs W., 2009, *Mol. Phys.*, accepted, DOI 10.1080/00268970903413350
- Blatt S. et al., 2008, *Phys. Rev. Lett.*, 100, 140801
- Calmet X., Fritzsche H., 2002, *Euro. Phys. J. C*, 24, 639
- Chengalur J.N., Kanekar N., 2003, *Phys. Rev. Lett.*, 91, 241302
- Cingöz A., Lapierre A., Nguyen A.-T., Leefer N., Budker D., Lamoreaux S.K., Torgerson J.R., 2007, *Phys. Rev. Lett.*, 98, 040801
- Cowie L.L., Songaila A., 1995, *ApJ*, 453, 596
- Darling J., 2004, *ApJ*, 612, 58
- Dent T., Stern S., Wetterich C., 2008, *Phys. Rev. D*, 78, 103518
- Edlen B., 1966, *Metrologia*, 2, 71
- Flambaum V.V., Kozlov M.G., 2007, *Phys. Rev. Lett.*, 98, 240801
- Griest K., Whitmore J.B., Wolfe A.M., Prochaska J.X., Howk J. C., Marcy G. W., 2010, *ApJ*, 708, 158
- Henkel C. et al., 2009, *A&A*, 500, 725
- Hinnen P.C., Hogervorst W., Stolte S., Ubachs W., 1994, *Canadian Journal of Physics*, 72, 1032
- Hollenstein U., Reinhold E., de Lange C.A., Ubachs W., 2006, *J. Phys. B*, 39, L195
- Ivanchik A., Petitjean P., Varshalovich D., Aracil B., Srianand R., Chand H., Ledoux C., Boissé P., 2005, *A&A*, 440, 45
- Ivanov T.I., Roudjane M., Vieitez M.O., de Lange C.A., Tchang-Brillet W.-Ü. L., Ubachs W., 2008, *Phys. Rev. Lett.*, 100, 093007
- Jenkins E.B., Peimbert A., 1997, *ApJ*, 477, 265
- Jennings D.E., Bragg S.L., Brault J.W., 1984, *ApJ*, 282, L85
- Kanekar N., 2008, *Mod. Phys. Lett. A*, 23, 2711
- Kanekar N. et al., 2005, *Phys. Rev. Lett.*, 95, 261301
- Kanekar N., Subrahmanyan R., Ellison S.L., Lane W.M., Chengalur J.N., 2006, *MNRAS*, 370, L46

King J.A., Webb J.K., Murphy M.T., Carswell R. F., 2008, Phys. Rev. Lett., 101, 251304  
 Ledoux C., Petitjean P., Srianand R., 2003, MNRAS, 346, 209  
 Levshakov S.A., Molaro P., Kozlov M.G., 2008, preprint (arXiv:0808.0583)  
 Liddle A.R., 2007, MNRAS, 377, L74  
 Marion H. et al., 2003, Phys. Rev. Lett., 90, 150801  
 Meshkov V.V., Stolyarov A.V., Ivanchik A.V., Varshalovich D. A., 2006, Sov. Phys. JETP Lett., 83, 303  
 Murphy M.T., Flambaum V.V., Muller S., Henkel C., 2008, Sci, 320, 1611  
 Murphy M.T., Flambaum V.V., Webb J.K., Dzuba V. V., Prochaska J. X., Wolfe A. M., 2004, Lecture Notes Phys., 648, 131  
 Murphy M.T., Tzanavaris P., Webb J.K., Lovis C., 2007, MNRAS, 378, 221  
 Murphy M.T., Webb J.K., Flambaum V.V., 2003, MNRAS, 345, 609  
 Murphy M.T., Webb J.K., Flambaum V.V., 2008, MNRAS, 384, 1053  
 Noterdaeme P., Ledoux C., Petitjean P., Le Petit F., Srianand R., Smette A., 2007, A&A, 474, 393  
 Noterdaeme P., Ledoux C., Petitjean P., Srianand R., 2008, A&A, 481, 327  
 Noterdaeme P., Petitjean P., Ledoux C., Srianand R., Ivanchik A., 2008, A&A, 491, 397  
 Peik E., Lipphardt B., Schnatz H., Schneider T., Tamm C., Karshenboim S.G., 2004, Phys. Rev. Lett., 93, 170801  
 Petitjean P., Ledoux C., Noterdaeme P., Srianand R., 2006, A&A, 456, L9  
 Philip J., Sprengers J.P., Pielage T., de Lange C.A., Ubachs W., Reinhold E., 2004, Canadian J. Chem., 82, 713  
 Prestage J.D., Tjoelker R.L., Maleki L., 1995, Phys. Rev. Lett., 74, 3511  
 Prochaska J.X., Wolfe A.M., 2009, ApJ, 696, 1543  
 Reinhold E., Buning R., Hollenstein U., Ivanchik A., Petitjean P., Ubachs W., 2006, Phys. Rev. Lett., 96, 151101  
 Rosenband T. et al., 2008, Sci, 319, 1808  
 Salumbides E.J., Bailly D., Khranov A., Wolf A.L., Eikema K.S. E., Vervloet M., Ubachs W., 2008, Phys. Rev. Lett., 101, 223001  
 Shelkovich A., Butcher R.J., Chardonnet C., Amy-Klein A., 2008, Phys. Rev. Lett., 100, 150801  
 Thompson R.I., 1975, Astron. Lett., 16, 3  
 Thompson R.I. et al., 2009, ApJ, 703, 1648  
 Tzanavaris P., Murphy M.T., Webb J.K., Flambaum V.V., Curran S. J., 2007, MNRAS, 374, 634  
 Tzanavaris P., Webb J.K., Murphy M.T., Flambaum V.V., Curran S. J., 2005, Phys. Rev. Lett., 95, 041301  
 Ubachs W., Buning R., Eikema K.S.E., Reinhold E., 2007, J. Molecular Spectrosc., 241, 155  
 Ubachs W., Eikema K.S.E., Hogervorst W., Cacciani P.C., 1997, J. Opt. Soc. America B, 14, 2469  
 Ubachs W., Reinhold E., 2004, Phys. Rev. Lett., 92, 101302  
 van Veldhoven J., Küpper J., Bethlehem H.L., Sartakov B., van Roij A.J.A., Meijer G., 2004, European Physical Journal D, 31, 337  
 Varshalovich D.A., Ivanchik A.V., Petitjean P., Srianand R., Ledoux C., 2001, Astron. Lett., 27, 683  
 Varshalovich D.A., Levshakov S.A., 1993, Sov. Phys. JETP Lett., 58, 237  
 Vogt S.S. et al., 1994, in Crawford D.L., Craine E.R., eds, Proc. SPIE Vol. 2198, Instrumentation in Astronomy VIII. p. 362  
 Wendt M., Reimers D., 2008, Euro. Phys. J. Special Topics, 163, 197  
 Wolfe A.M., Brown R.L., Roberts M.S., 1976, Phys. Rev. Lett., 37, 179

## APPENDIX A: MONTE CARLO TEST OF FITTING ALGORITHM TO DETERMINE $\Delta\mu/\mu$

The fiducial fit performed on the spectrum of J2123–0050 to determine  $\Delta\mu/\mu$  is a fairly large and complex one. It contains more fitted spectral pixels and more fitted parameters than most, if not all, previous fits of its kind in the literature. Furthermore, the fitted parameters are not all free and independent, but are tied together in a variety of physically meaningful ways. Therefore, to ensure that the fitting code `vpfit` determines  $\Delta\mu/\mu$  correctly in this context, we performed a Monte Carlo test using simulated spectra pro-

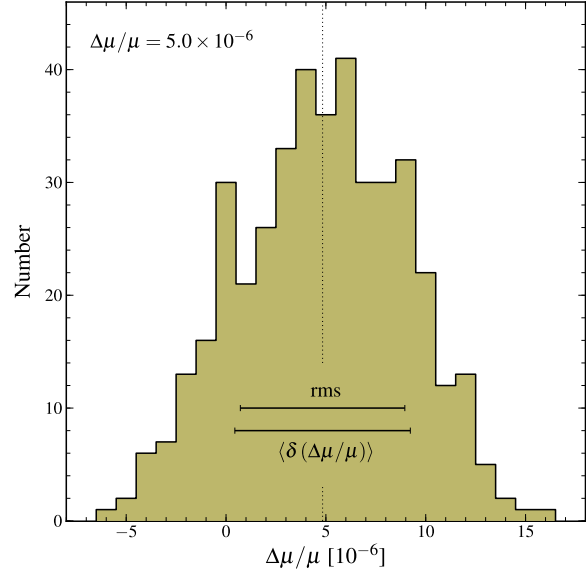


**Figure A1.** 420 Monte Carlo simulations of the fiducial 4 component absorption model used in our analysis. The value of  $\Delta\mu/\mu$  returned from the simulated spectra (vertical dotted line) corresponds well to the input value,  $+5 \times 10^{-6}$ . The mean 1- $\sigma$  error and the standard deviation are shown to be consistent.

duced from the fiducial fit we established to the real data. That is, each simulated spectrum is produced simply by taking the fit with 4 molecular velocity components, plus all the fitted Lyman- $\alpha$  forest lines, interloping metal lines, local continuum and zero flux level adjustments, and adding Gaussian noise with a  $\sigma$  of 0.8 times the error array of the real spectrum. The artificially high SNR in the simulations was used to ensure that Lyman- $\alpha$  blends that were only marginally statistically required in the fit to the real spectrum were not removed statistically when fitting the simulated versions.

Each simulated spectrum was then fitted with `vpfit` with initial guess parameters set to be those used to produce the simulated spectrum. An input value of  $\Delta\mu/\mu = +5 \times 10^{-6}$  was used to test whether `vpfit` recovered that value when started from an initial guess of zero. Figure A1 shows the results of fitting 420 simulated spectra. The mean 1- $\sigma$  uncertainty derived on individual  $\Delta\mu/\mu$  measurements is  $4.4 \times 10^{-6}$  which is the expected value given the value of  $5.5 \times 10^{-6}$  from the real spectrum and a scaling of 0.8 times its flux errors. This corresponds well to the RMS of  $4.1 \times 10^{-6}$  for the 420  $\Delta\mu/\mu$  measurements; it may even be that the individual uncertainties returned by `vpfit` are slightly conservative. The mean  $\Delta\mu/\mu$  value retrieved is  $4.8 \times 10^{-6}$ .

This paper has been typeset from a  $\text{\LaTeX}$  file prepared by the author.

## APPENDIX B: SUPPORTING INFORMATION

Figure B1 is the complete version of Fig. 1. It will appear in the online version of this paper, not in the printed version. Table B1, the complete version of Table 1, is provided in the online version only as a machine-readable ASCII file.

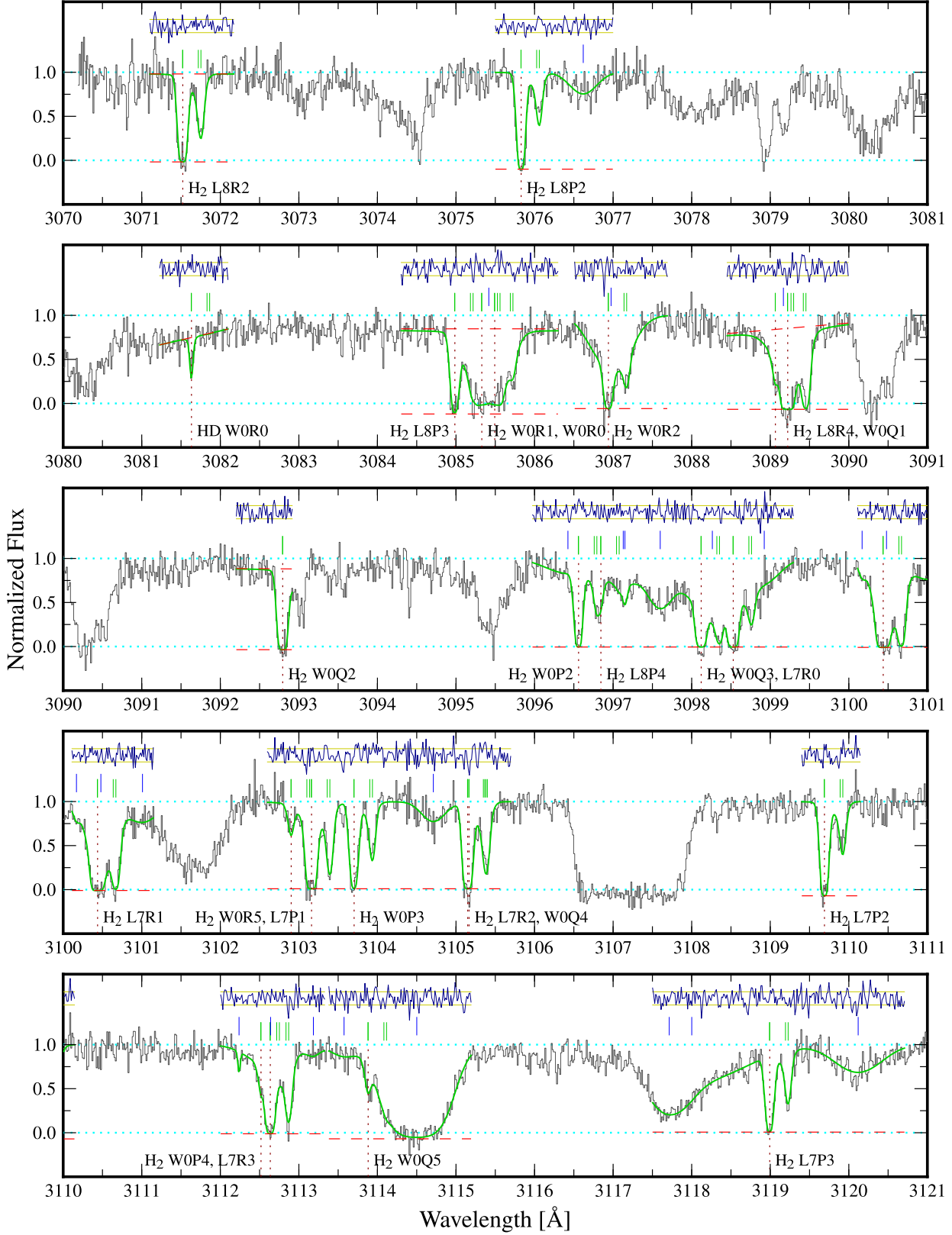


**Figure B1.** All regions of the J2123–0050 Keck spectrum fitted simultaneously in our analysis. The spectrum (black histogram) is normalized by a nominal continuum (upper dotted line) fitted over large spectral scales. Local linear continua (upper dashed lines) and zero levels (lower dashed lines) are fitted simultaneously with the H<sub>2</sub>/HD and broader Lyman- $\alpha$  lines. The fits are shown with solid grey/green lines. H<sub>2</sub>/HD transitions are labelled and their constituent velocity components are indicated by grey/green tick-marks immediately above the spectrum. Higher above the spectrum are tick-marks indicating the positions of Lyman- $\alpha$  lines (blue) and Fe II lines (red). Note that the metal-line velocity structure is constrained with the Fe II  $\lambda 1608$  Å transition shown in the final panel of the figure. The residual spectrum (i.e. [data] – [fit]), normalized to the 1- $\sigma$  errors (faint, horizontal solid lines), is shown above the tick-marks.



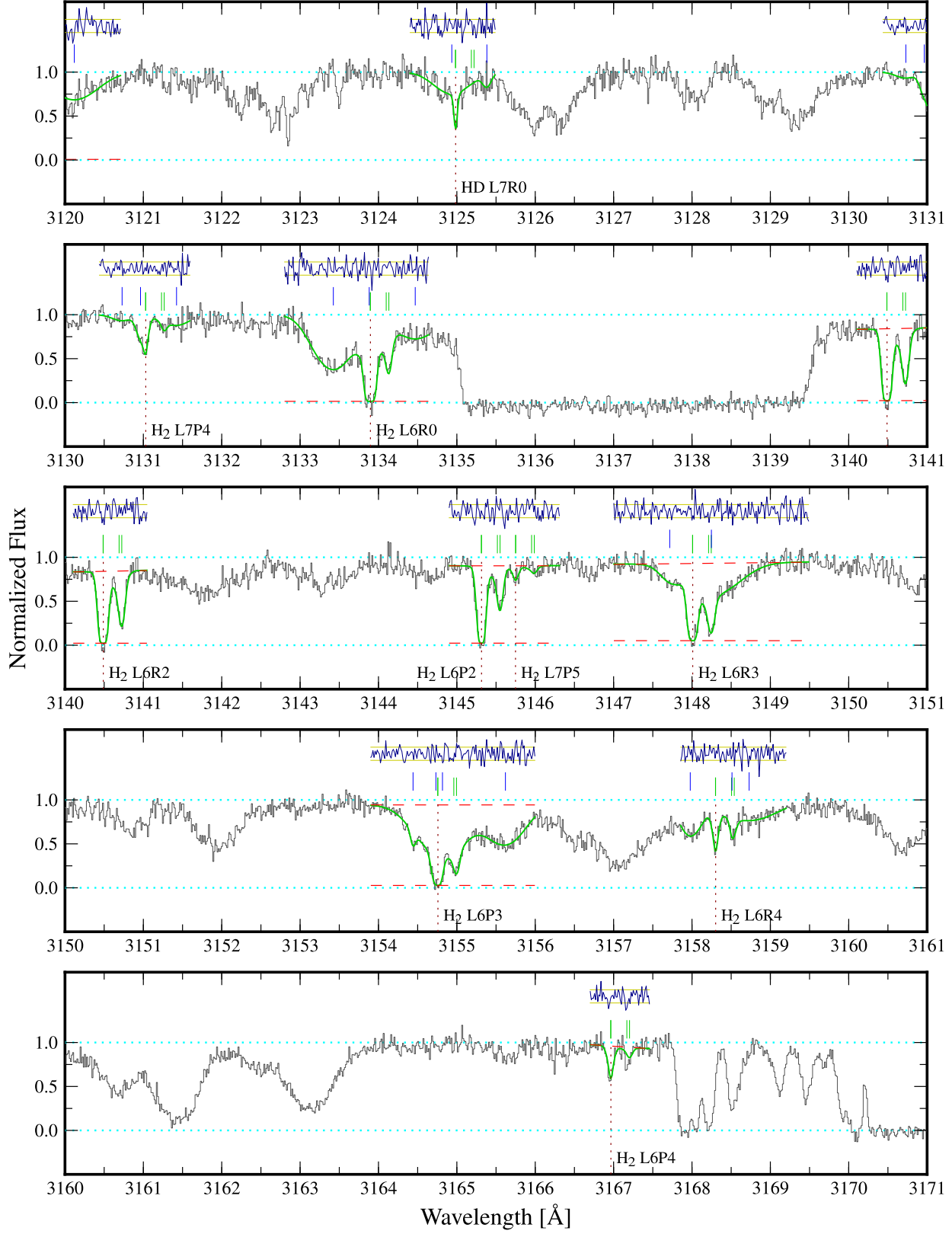


Figure B1 – continued

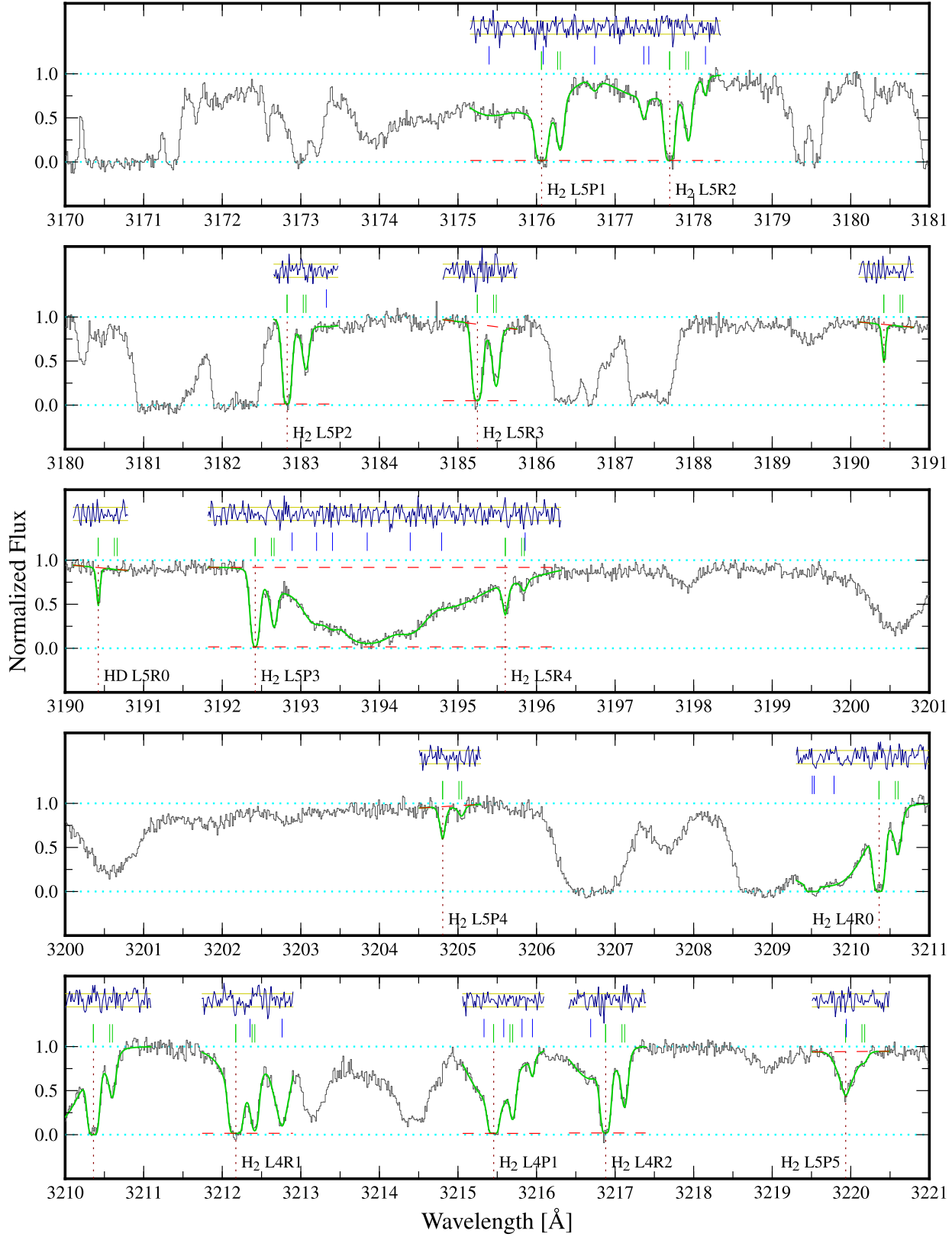


Figure B1 – continued

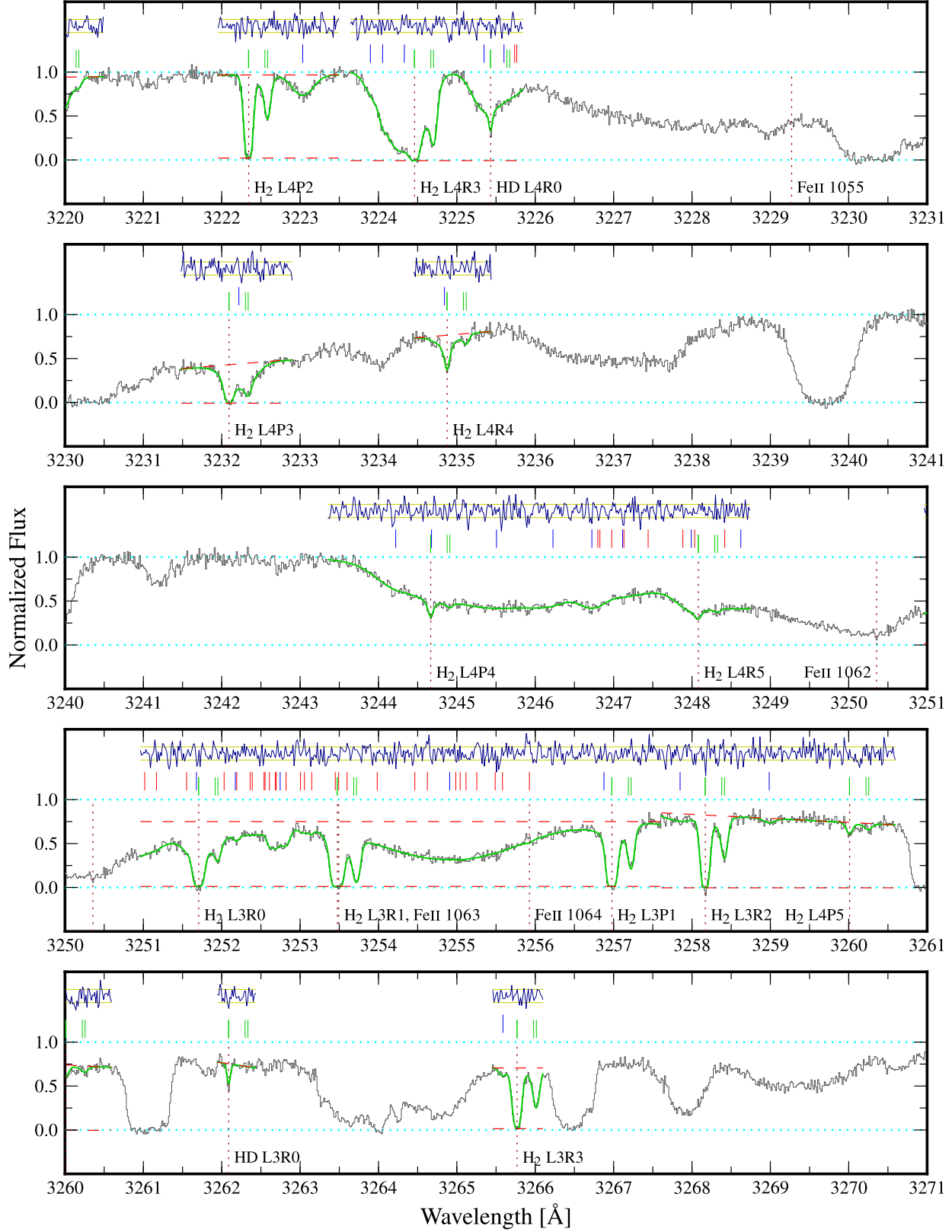


Figure B1 – continued

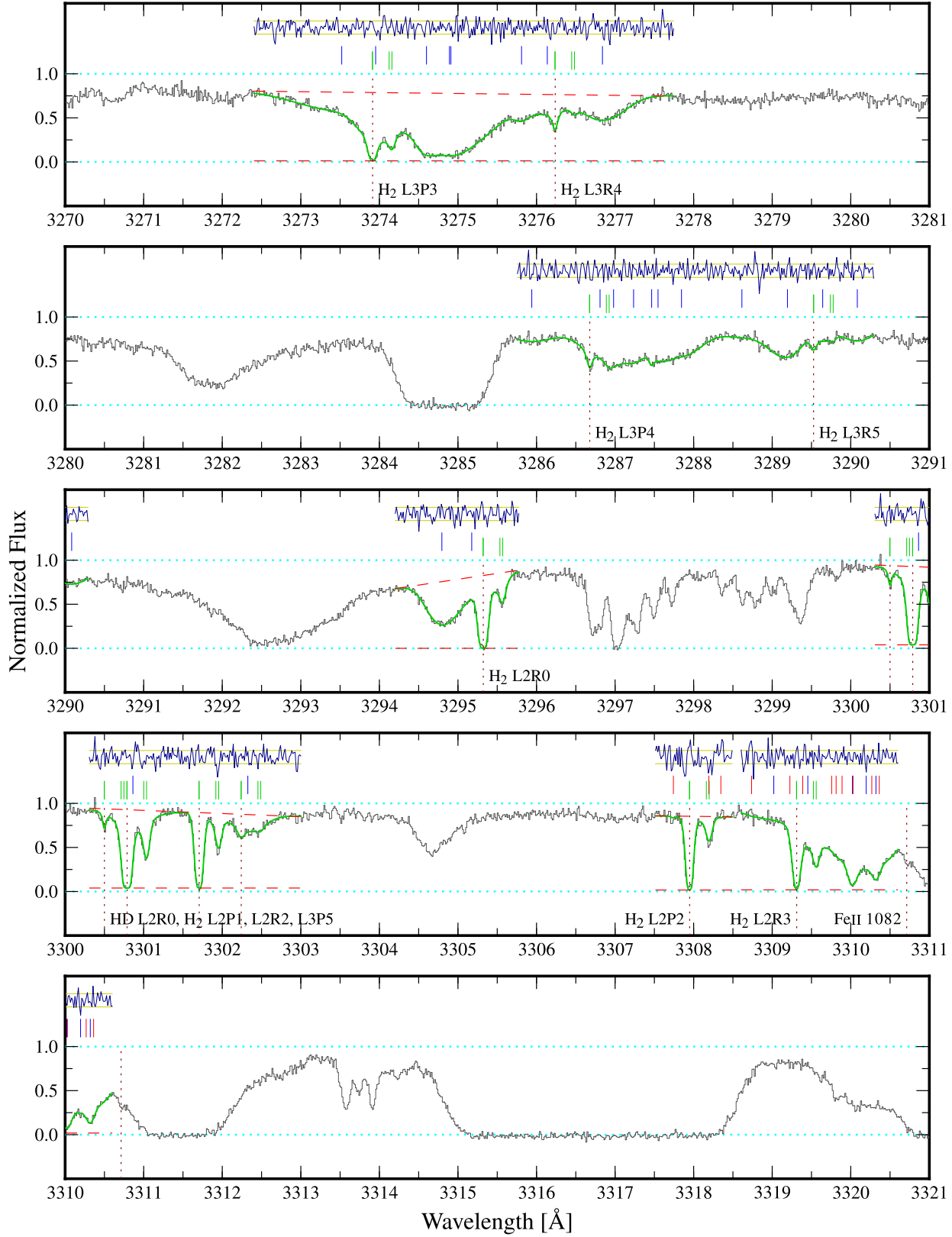


Figure B1 – continued



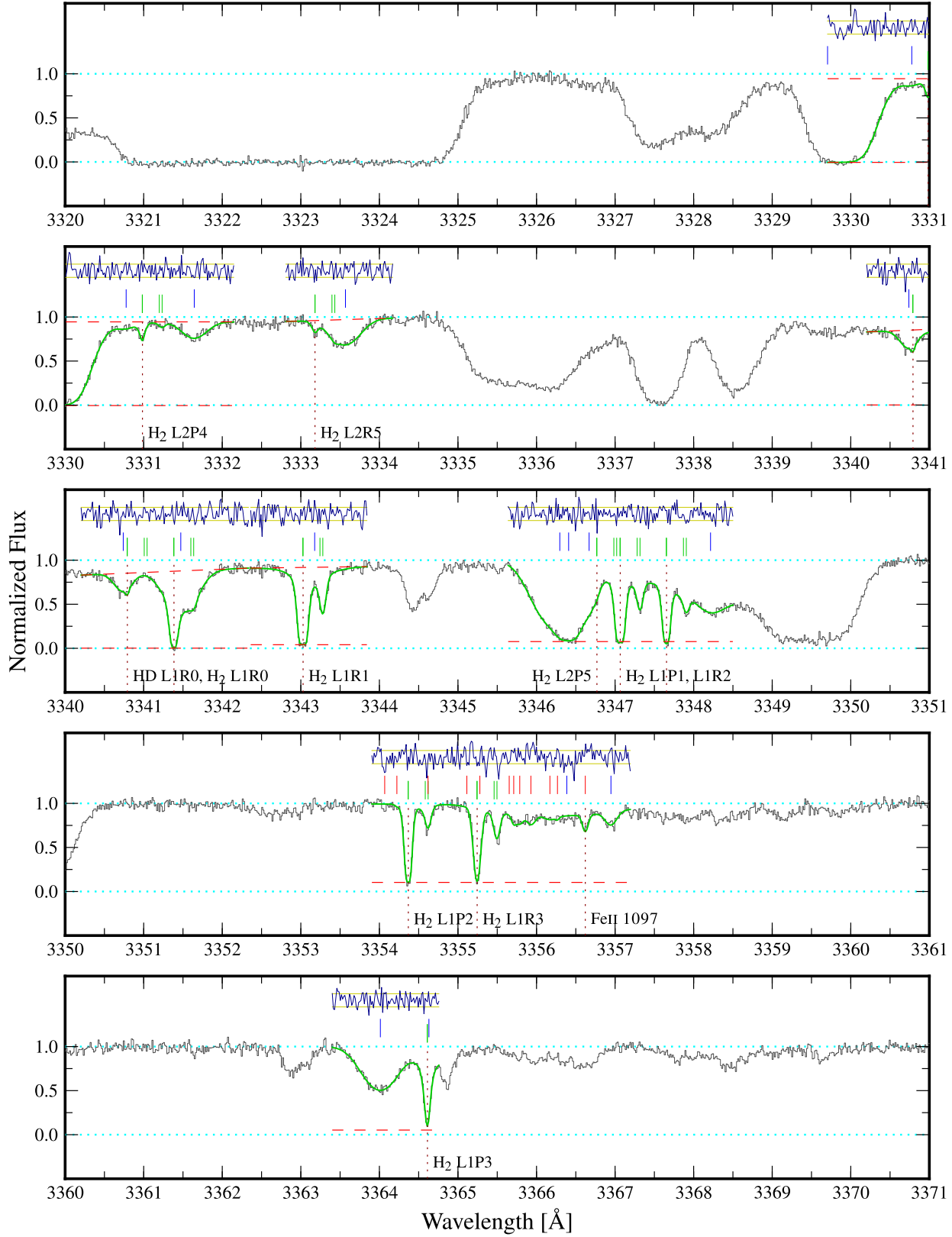
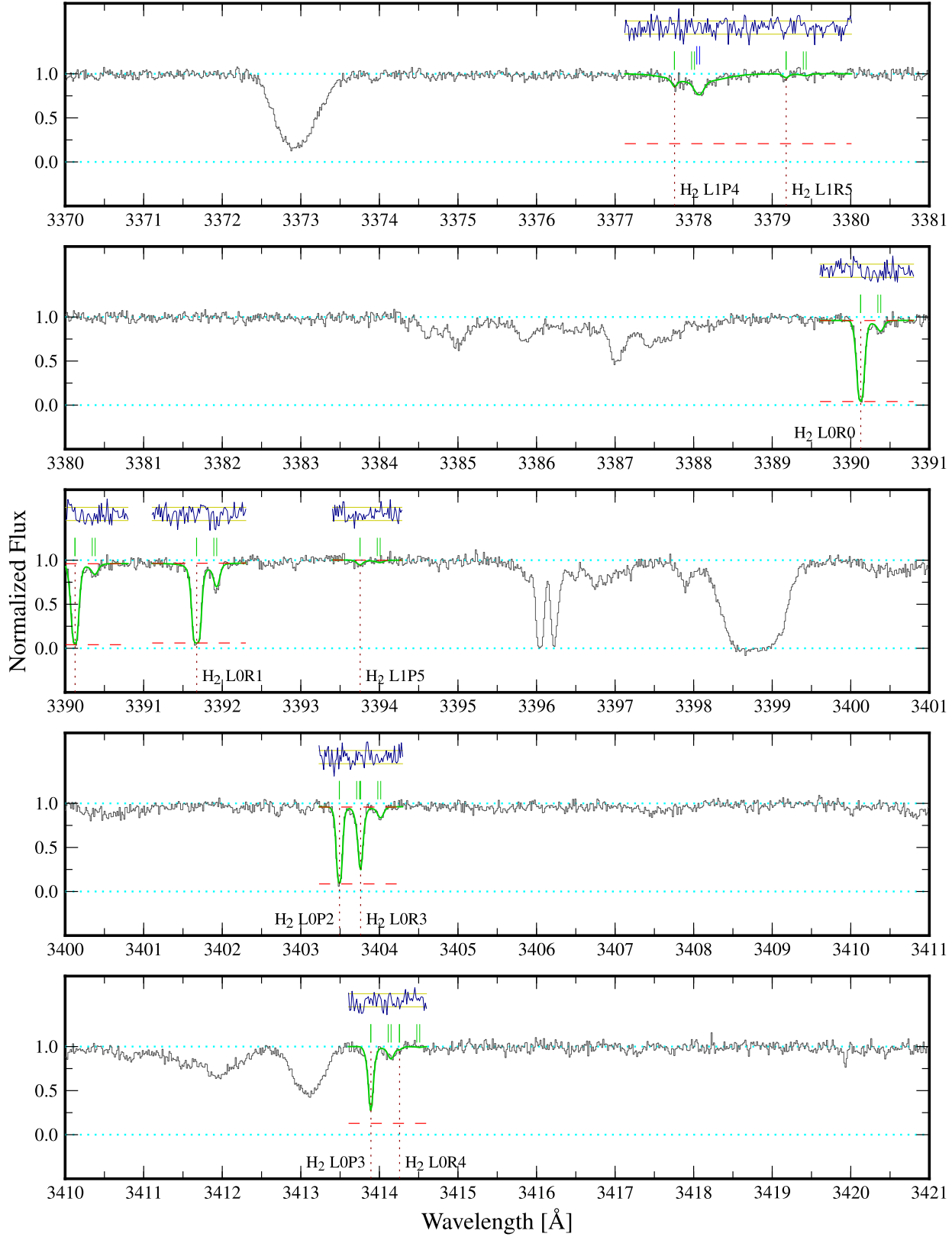


Figure B1 – continued

Figure B1 – *continued*

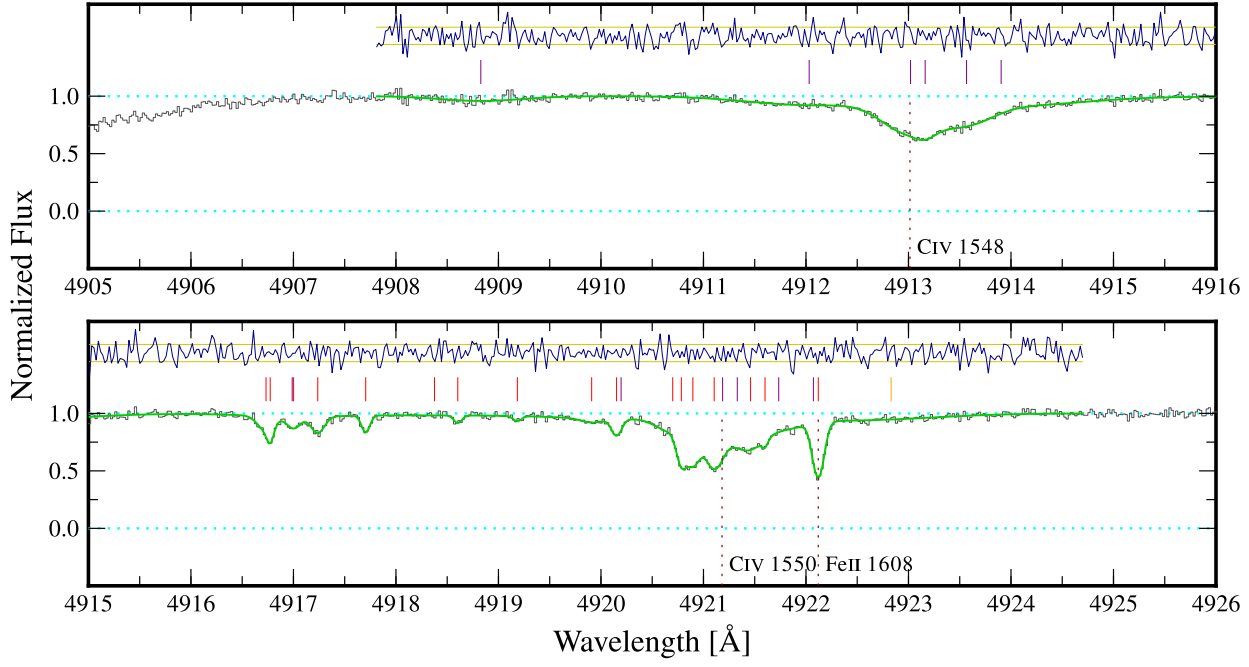


Figure B1 – continued